Silicon Electrolyte Interface Stabilization (SEISta)
Quarter 2 FY19

Anthony Burrell

National Renewable Energy Laboratory
15013 Denver West Parkway
Golden, CO 80401
Phone: (303) 384-6666
E-mail: anthony.burrell@nrel.gov

Brian Cunningham, DOE-EERE-VTO Program Manager

Hybrid Electric Systems, Battery R&D
Phone: (202) 586-8055
E-mail: brian.cunningham@ee.doe.gov

Table of Contents

Project Introduction

This report documents the Silicon Electrolyte Interface Stabilization team's approach in 1) characterizing the early-stage silicon-electrolyte interphase (SEI) including progress on identifying the specific reaction pathways present in the formation of the SEI layer, and 2) establishing a procedure for measuring SEI growth rate at fixed potentials and different cycling regimes.

Silicon is a viable alternative to graphitic carbon as an electrode in lithium-ion cells and can theoretically store >3,500 mAh/g. However, lifetime problems have been observed that severely limit its use in practical systems. The major issues appear to involve the stability of the electrolyte and the uncertainty associated with the formation of a stable SEI at the electrode. Recently, calendar-life studies have indicated that the SEI may not be stable even under conditions where the cell is supposedly static. Clearly, a more foundational understanding of the nature of the silicon/electrolyte interface is required if we are to solve these complex stability issues. A new multi-lab consortium has been formed to address a critical barrier in implementing a new class of materials used in lithium-ion batteries that will allow for smaller, cheaper, and better-performing batteries for electric-drive vehicles. This consortium, named the Silicon Electrolyte Interface Stabilization (SEISta) project, was formed to focus on overcoming the barrier to using such anode materials. Five national laboratories are involved: the National Renewable Energy Laboratory (NREL), Argonne National Laboratory (ANL), Lawrence Berkeley National Laboratory (LBNL), Oak Ridge National Laboratory (ORNL), and Sandia National Laboratories (SNL).

The SEISta project was specifically developed to tackle the foundational understanding of the formation and evolution of the solid-electrolyte interphase on silicon. This project will have as its primary goal an understanding of the reactivity of the silicon and lithiated silicon interface with the electrolyte in lithium-ion systems. It consists of researchers from multiple national laboratories (NREL, ANL, LBNL, ORNL, and SNL) working toward clear unified goals. The Silicon Deep-Dive team, which focuses on the science and technology barriers in functional electrodes, is a critical partner in this work. Many of the researchers are shared between both teams, and we hold joint meetings to ensure effective communication between the teams.

The current goals of SEISta are:

Quarter 1 Milestone: Have determined if the pristine surface of the silicon influences the composition and the function of the SEI after 1, 10, and 50 cycles (XPS, SIMS, IR, and Raman, STEM, SSRM). (100% complete)

Quarter 2 Milestone: Have determined that the nature of the silicon surface can affect the composition, function, and thickness of the SEI. (100% complete)

Quarter 3 Milestone: Have determined how water concentration (as a function of water content up to 100 ppm) in the electrolyte affects SEI thickness and composition (electrochemistry, spectroscopy, impedance) of the SEI formed at 1.5, 1.0, 0.7, 0.4, 0.15, and 0.05 V vs Li/Li+.

Quarter 4 Milestone: Have determined the nature of the soluble SEI components that are formed over 10 cycles and that are soluble in the Gen 2 electrolyte.

Approach

The SEISta team works to ensure that protocols for sample preparation, experimental design, and implementation as well as data reporting are consistent across the whole team. Each laboratory is working toward the same set of quarterly milestones using its own specific talents and capabilities in a concerted effort with the other team members. This joint focus results in multiple researchers interacting to produce and analyze data to ensure that individual experimental variations will not lead to erroneous results. Critical to the success of this effort is the use of standard samples that can be shared by all parties. In addition to weekly whole-team video presentations, we have held on-site face-to-face meetings each quarter for all team members and other interested parties to brainstorm and sort out issues with existing experiments and jointly develop new experimental plans.

Objectives

The critical issues that SEISta is attempting to determine are:
- What are the properties of the lithiated silicon/electrolyte interface?

- What is the silicon SEI actually made of and what reactions are contributing to it?

- How fast does the silicon SEI grow?

- Does it stop growing?

- Is it soluble?

- Can it be stabilized?

For FY19, the team continues to focus on three broad tasks:

Materials Standardization – This task is critical to the development and deployment of standardized samples and experimental procedures across the team. We will continue to provide full characterization to any new sample that is to be used for SEI studies to ensure reproducibility and full understanding of the material. This quarter's work focused on developing new oxide coatings and methods to control the thickness and density of oxide samples. In addition, work on the silicon nanoparticles has made progress with the enhancement of the materials collection and handling system in the plasma reactor. *Although this work dominated the early part of the project and is still critical to its success, it is now only a minor part of the work and this is reflected in the relative balance of this quarterly report.*

Model Materials Development and Characterization – The nature of the electrode-electrolyte interaction in silicon electrodes is at the heart of the formation and stability of the SEI. The inherent chemical reactivity of silicon with common electrolytes has been a focus for this team and will be a primary focus moving to quarter 2. The synthesis of well-defined silicon nanoparticles and the different chemical markups of lithiated silicon surfaces is being probed by preparing model compounds and thin films that may/can exist in silicon anodes. Lithium silicides, silicates, and other inorganic material (LiF, Li_2O) are being prepared, and their reactivity with electrolytes is being determined. These materials also act as standard spectroscopy samples for the researchers who are looking at the formation of the SEI on different silicon materials.

SEI Characterization – The overall objective for SEISta is to understand the nature and evolution of the SEI on silicon anodes. The materials standardization and model compounds will enable the researchers to systematically investigate the formation of the solid-electrode interphase using a wide variety of the spectroscopy techniques—from different optical, microscopy, and electrochemistry—to determine how the SEI forms based on the nature of the silicon surface, and how it evolves over time. This section of work will continue to grow in scope as we move beyond the sample-characterization phase of the project and toward understanding the nature and evolution of the SEI. *This part of the project now represents the bulk of the work and, as such, this quarterly report is largely reporting on work leading to this outcome.*

SEISta Milestones FY19 Silicon Electrolyte Interface Stabilization (SEISta)

SEISta Team

Background

The overall objective of the SEISta project is to better understand the formation and evolution of the solid-electrolyte interphase (SEI) on silicon anodes. Silicon is a viable alternative to graphitic carbon as an electrode in lithium-ion cells and can theoretically store >3,500 mAh/g. However, lifetime problems have been observed that severely limit its use in practical systems. The major issues appear to involve the stability of the electrolyte and the uncertainty associated with the formation of a stable SEI at the electrode. Recently, calendar-life studies have indicated that the SEI may not be stable even under conditions where the cell is supposedly static. Clearly, a more foundational understanding of the nature of the silicon/electrolyte interface is required if we are to solve these complex stability issues. A multi-lab consortium has been formed to address a critical barrier in implementing a new class of materials used in lithium-ion batteries that will allow for smaller, cheaper, and better-performing batteries for electric-drive vehicles. This consortium—the Silicon Electrolyte Interface Stabilization (SEISta) project—was formed to focus on overcoming the barrier to using such anode materials. Five national laboratories, led by the National Renewable Energy Laboratory (NREL), are involved: NREL, as well as Argonne (ANL), Lawrence Berkeley (LBNL), Oak Ridge (ORNL), and Sandia National Laboratories (SNL).

Quarter 2 Milestone:
Have determined that the nature of the silicon surface can affect the composition, function, and thickness of the SEI. (100% complete)

Part 1. The SiO₂ Interface

Silicon Electrolyte Interface Stabilization (NREL) - FY19, Q2

Elisabetta Arca, Manuel Schnabel, Paul Stradins, Tony Burrell, Glenn Teeter (PI), NREL, Golden, CO

Background

In FY18, NREL researchers developed a capability to perform *in situ* lithiation of model $SiO_2/Si(001)$ anodes using a low-energy Li^+ ion gun, while monitoring chemical evolution with X-ray photoelectron spectroscopy (XPS). This virtual-electrode approach provides an ability to track chemical and phase evolution in real time while driving Li^+ ionic current through battery materials and structures. When applied to samples that have never been exposed to an electrolyte, it enables detailed studies of inorganic constituents of the Si-anode solid-electrolyte interphase (SEI), specifically those that exist within the ternary Li-Si-O phase system.

This virtual electrode *in situ* lithiation technique provides:
- A method to experimentally map SEI-relevant phases in the Li-Si-O ternary-phase system.
- Information on the transformation of SiO_x surface oxides into silicate phases (Li_xSiO_y), and of Si^0 into silicide phases (Li_xSi), and on subsequent phase evolution as a function of lithiation.
- Insights into the roles that silica surface phases (SiO_2, SiO_x) play in determining electronic vs. ionic conductivities, which, in turn, influence electrolyte-reduction processes.
- A methodology for assessing chemically resolved overpotentials for individual phases observed in the SEI.

Results

In Q2, we continued *in situ* lithiation studies of model-system Si anode materials [5-nm $SiO_2/Si(001)$ wafer] to further understand formation and evolution of inorganic components of the silicon solid-electrolyte interphase. The SiO_2 films were prepared at NREL on highly p-doped Si(001) substrates and were transferred through air into the instrument for XPS measurements. Li^+ ions were supplied via a low-energy ion gun incorporated onto the XPS instrument, with an incident energy of 10 eV and typical current densities in the range 200–500 nA/cm^2. During the *in situ* lithiation experiment, surface composition and chemical states were monitored in real time with XPS to probe the evolution of inorganic phases present at the exposed surface. The XPS information depth using Al-Kα X-ray excitation (hv = 1486.7 eV) is on the order of 10 nm, which allows *in situ* XPS measurements to track compositional changes in both the SiO_2 film and in the underlying near-surface bulk silicon wafer.

A key goal of *in situ* lithiation experiments performed in Q2 was to understand effects of visible-light illumination on the evolution of inorganic SEI components. After noting some discrepancies in previous experiments, we determined that light-bias can have substantial effects on phase evolution, so controlled experiments were performed with light bias supplied by a white-light LED (ThorLabs Solis-3C), which supplied a power density ~ 10 mW/cm^2.

Figure 1 summarizes *in situ* lithiation results with and without applied light bias. Surprisingly, there are substantial differences between the two cases. Most notably, in the no-light-bias case, the majority of SiO_2 that is present initially (see the O 1s and Si 2p features in Fig 1(a) at ~536 eV and ~106.5 eV, respectively) persists throughout the experiment and remains, even after all Si^0 in the underlying substrate within the XPS information depth has been converted to a Li_xSi phase. This indicates that i) Li^+ ion conductivity through SiO_2 is sufficiently high that it does not completely inhibit lithiation of the underlying silicon; and ii) Li_xSi formation is kinetically favored over Li_xSiO_y formation, at least under conditions tested in this experiment. It should be noted that a small component of the SiO_2 is converted to a silicate phase in the no-light-bias case, presumably via Eq. 1 (or a similar reaction).

$$xLi^+ + SiO_2 + xe^- \rightarrow Li_xSiO_2 \qquad\qquad (1)$$

Previously reported angle-resolved XPS measurements demonstrated that the observed Li_xSiO_y phase forms at the surface, on top of the SiO_2 layer, indicating that there must be a non-negligible electronic conductivity present in the SiO_2 initially that facilitates formation of the silicate phase.
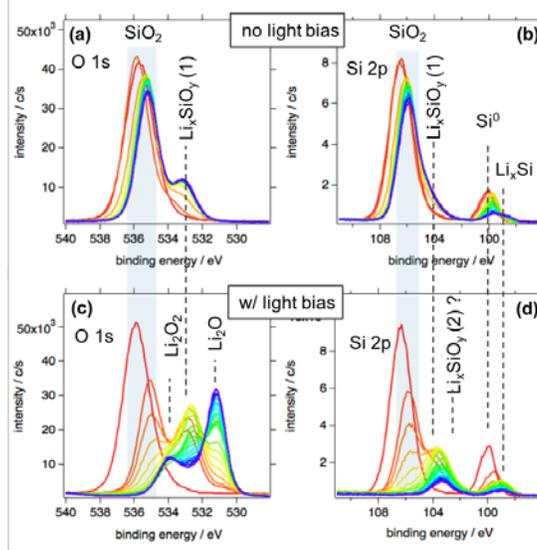
Figure 1. Summary of XPS measurements performed during *in situ* lithiation of 5-nm SiO_2/Si(001) wafer anodes. Panels (a) and (b) represent O 1s and Si 2p core levels, respectively, acquired during *in situ* lithiation in the dark. Panels (c) and (d) represent the same set of measurements performed with 10 mW/cm² white-light bias.

The phase evolution observed for the light-bias case is summarized in more detail in Fig. 2. Here, it can be seen that in contrast to the no-light-bias case, the SiO_2 is fully transformed into Li_xSiO_y and other phases. Specifically, there is clear evidence for a silicate phase [labeled Li_xSiO_y (1)] characterized by O 1s and Si 2p peaks at 532.7 eV and 101.8 eV, respectively. In addition, a small peak grows in the Si 2p core-level spectrum at ~102 eV that might be associated with a second silicate phase [Li_xSiO_y (2)], although it should be noted that no corresponding O 1s feature is clearly resolved, possibly due to interferences with much larger peaks from the other oxygen-containing phases that are also present. Peaks are also observed in the O1s spectrum at 531 eV and 534 eV, which are tentatively identify as Li_2O and Li_2O_2 (or possibly LiOH) [1].

To further elucidate the role of light bias on *in situ* lithiation results, a curve-fitting exercise was performed to extract band-bending phenomena within the SiO_2/Si(001) heterostructure directly from XPS spectra. Figure 3(a) illustrates the overall shift and broadening observed in the Si 2p core levels that accompanies application of Li^+ current bias. These effects are seen in both the SiO_2 and Si^0 core levels, and they are clear evidence that Li^+ current bias induces an electrochemical potential gradient in the SiO_2/Si(001) anode within the XPS information depth. For the spectrum measured with white-light bias, photoexcitation within the silicon-wafer bulk creates a photovoltage that tends to flatten the bands. Therefore, the green spectrum in Fig. 3(a) represents a basis set for the Si 2p core-level peak associated with both the SiO_2 overlayer and the underlying Si(001) wafer that can be used to determine the degree of band bending in each layer. The curve-fitted spectrum in Fig. 3(a) was generated by summing shifted spectral components attenuated by the electron inelastic mean free path as a function of depth from the sample surface, as illustrated in Fig. 3(b). The curve-fitting parameters [open circles, Fig. 3(b)] reveal the extent of band bending in the SiO_2 and near-surface Si(001). The linear electrochemical gradient in the SiO_2 layer is about 3.2 MeV/cm, which provides the driving force for Li^+ migration into the underlying silicon.
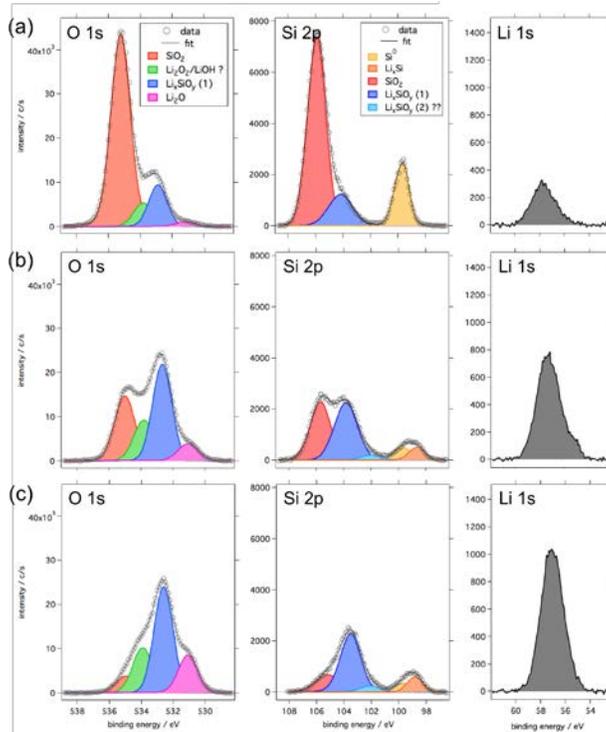
Figure 2. Summary of phase evolution for *in situ* lithiation of 5-nm SiO$_2$/Si(001) wafer anode with applied white-light bias (10 mW/cm^2) for (a) early-, (b) mid-, and (c) late-stage lithiation. In the presence of light bias, the SiO$_2$ features that are initially present in the O1s and Si 2p core-level spectra are progressively attenuated, and concurrently, the Si^0 peak is transformed into one associated with a Li$_x$Si phase.
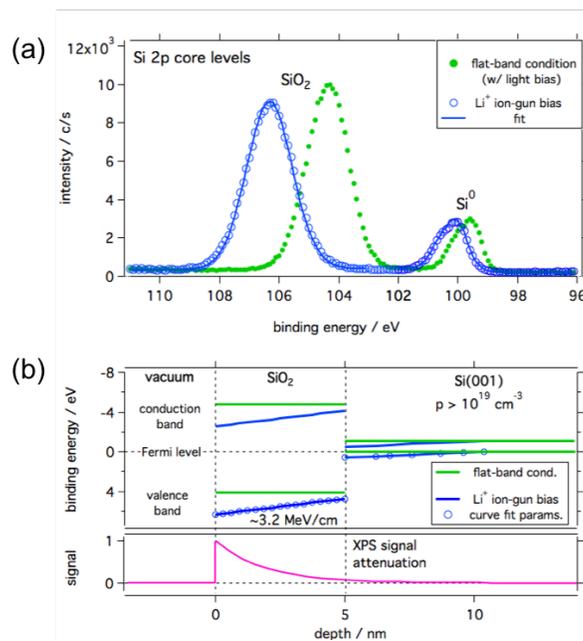
Figure 3. (a) Si 2p core-level XPS spectra acquired with applied white-light bias and with Li$^+$ ion-gun current bias. (b) Band diagrams inferred from the XPS spectra. The open circles in panel (b) represent curve-fitting parameters extracted from the Si 2p spectrum in panel (a).

Other XPS measurements (not shown) also revealed that light bias alone results in a change in band bending at the free surface, indicating that photoexcitation in the Si(001) wafer generates electron-hole pairs, with corresponding quasi-Fermi-level splitting that manifests as a surface photovoltage that shifts all measured XPS core levels. For the p^+-doped Si(001) wafer samples studied, we observed that 1) both no-light-bias and Li^+ current-bias conditions produced significant downward band bending in the Si(001) wafer near the SiO_2/Si(001) interface, and 2) light-bias-only conditions appeared to flatten the bands, as illustrated in Fig. 3(b). This condition would tend to sweep photogenerated electrons toward the SiO_2/Si(001) interface, where they would be available to participate in an interfacial reaction like that represented in Eq. (1). This photoexcitation mechanism explains the observed differences in light-bias on vs. off illustrated in Fig. 1: the application of light bias increases the population of electrons available at the SiO_2/Si(001) interface, which, in turn, facilitates interfacial reactions similar to Eq. (1). In the absence of light bias, evidently the population of electrons near the interface is low enough that Li_+ ions must travel into the Si(001) wafer before they can recombine with an electron and react to form Li_xSi.

Conclusions

The studies reported here demonstrate several key findings related to formation of inorganic SEI components on SiO_2/Si(001) model-system samples:

- Li^+ ion conductivity through thermally grown 5-nm-thick SiO_2 films is sufficiently high that Li^+ transport is not completely hindered to the underlying silicon.
- For *in situ* lithiation experiments performed in the dark, the majority of SiO_2 that is initially present persists, even after all Si^0 within the XPS information depth has been converted to a Li_xSi phase.
- The substantial differences observed for *in situ* lithiation experiments performed with applied light bias can be understood in terms of the effects of the photogenerated electron population on SiO_2/Si(001) interfacial reactions.

References

[1] K.N. Wood, G. Teeter, ACS Appl. Energy Mater. **1** (2018) 4493–4504.

SEISta (Analytical Microscopy and Imaging Group, NREL)

Caleb Stetson, Yanli Yin, Manuel Schnabel, Andrew Norman, Chun-Sheng Jiang, Mowafak Al-Jassim (NREL)

Introduction

The solid-electrolyte interphase (SEI) formed on Si has been shown to be highly variable; composition, thickness, and function have displayed dependence on the model Si anode system, electrochemical conditions, and original Si surface. In this quarter, investigation focuses on investigating how the nature of the silicon surface affects the composition, function, and thickness of SEI. Model systems presented in this study include native SiO_x on Si wafer and thermally grown SiO_2 on Si wafer.

Results

Initial cycling conditions to investigate the differences between native SiO_x and 5-nm thermally grown SiO_2 were a fixed lithiation current density of 6.82 µA cm^{-2} until a cutoff voltage of 10 mV was reached. Delithiation was carried out at the same current density to a cutoff voltage of 1.5 V. 50 cycles were carried out under these conditions. The fixed current density was applied to lithiate for 10 minutes at 115 mV after the 50 cycles. Cells were disassembled immediately and rinsed in DMC for two minutes then dried in the glovebox antechamber for one hour. Airless transfer was then carried out and samples were immediately characterized with Atomic force microscopy (AFM) and Scanning spreading resistance microscopy (SSRM).
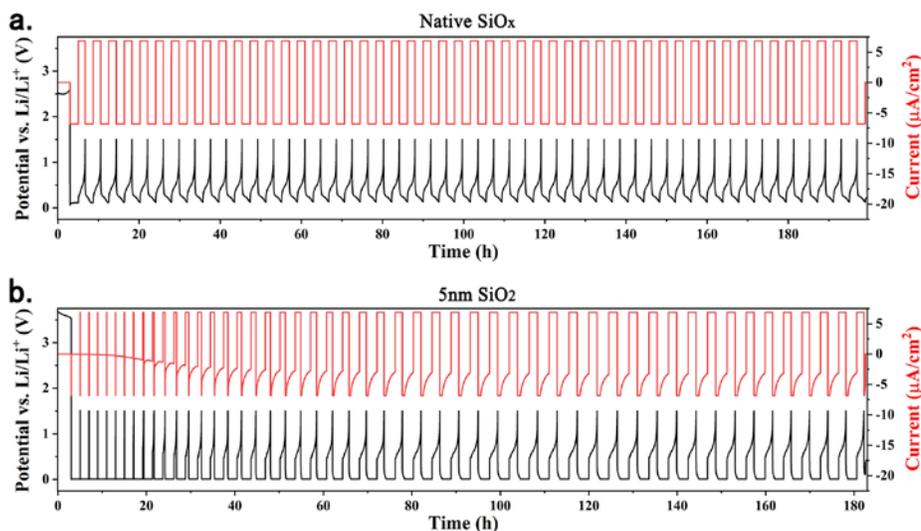
Figure 1. (a) Current and voltage vs. time for 50 cycles on the native SiO_x model system. (b) Current and voltage vs. time for 50 cycles on the 5-nm thermally grown SiO_2 model system.

As seen in the Figure 1, the 5-nm thermally grown SiO_2 inhibits lithiation and delithiation for the initial cycles. However, after ~20 cycles, the surface appears to "activate," allowing for lithiation and delithiation of the anode material. To further investigate this behavior, cycling conditions were changed to allow for lithiation potentials below 0 V vs. Li/Li$^+$ on varied thicknesses of the thermally grown SiO_2 (1.4, 2.1, 3.2, 4.3, and 5.2 nm).

Native SiO_x appears to cycle uniformly under most conditions, but for thermally grown SiO_2, Li diffusion is inhibited by thicker oxide films. On thinner SiO_2 films with thicknesses less than ~5 nm, uniform cycling and SEI formation appears to occur. For thicker SiO_2 films, inhomogenous lithiation occurs, originating and

9

expanding from an initial site, likely due to defect structures or porosity that facilitate Li diffusion. AFM was used to study the surface morphology of the zones, whereas SSRM was employed to profile the electronic properties of SEI and locate the interface with Si.
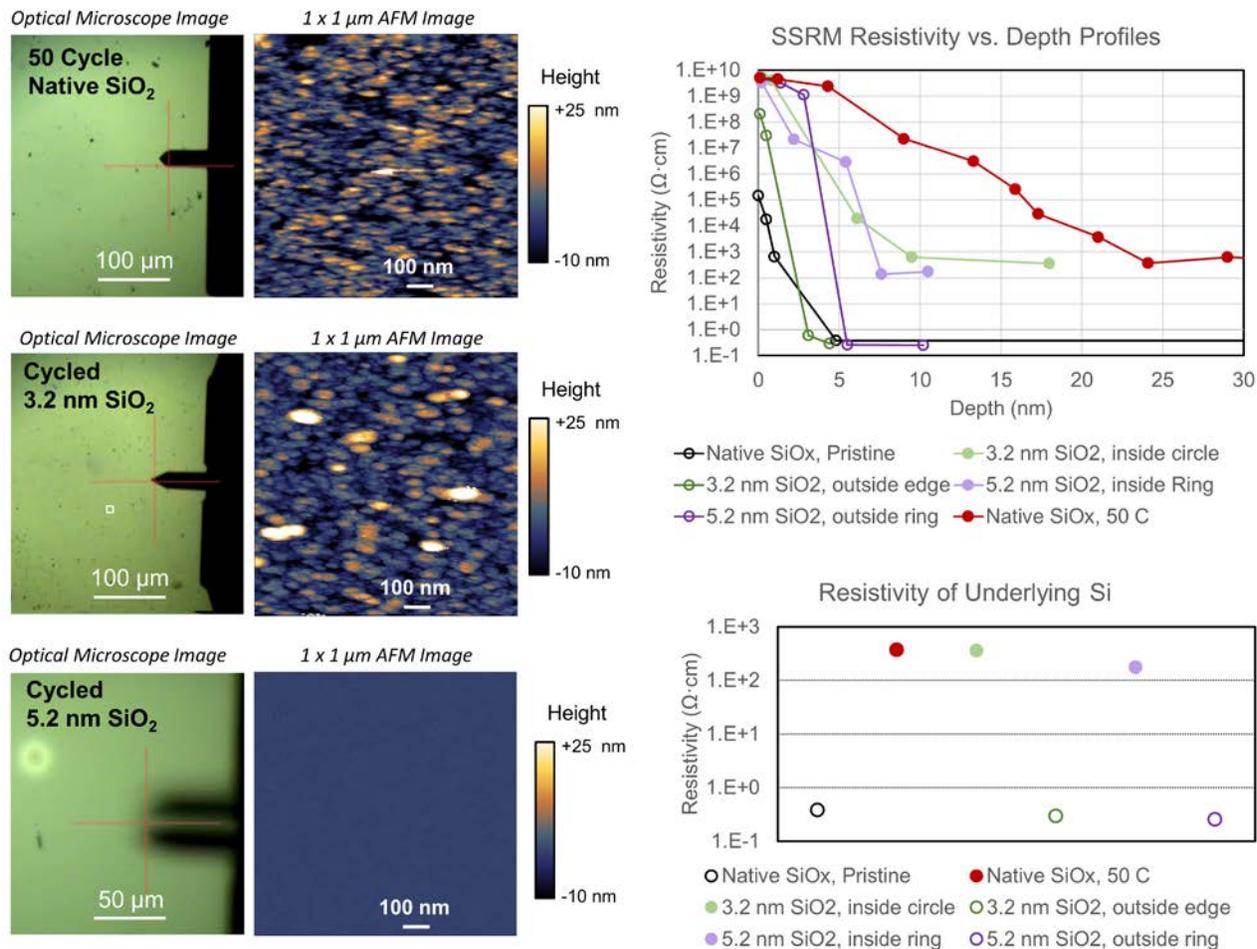
Figure 2. AFM instrument optical microscope images (left column) and 1x1 µm AFM images (middle column) from three representative samples: cycled native SiO_x, cycled 3.2-nm SiO_2, and cycled 5.2-nm SiO_2. Uniform lithiation/delithiation and SEI formation appear to form on the first two samples, but highly nonuniform SEI formation occurs on the final sample. SSRM resistivity vs. depth profiles (upper right panel) indicate comparative analysis for a pristine native SiO_x reference, a cycled native SiO_x SEI after 50 cycles, and two regions for each of the two SiO_2 samples, one active and one inactive through cycling. In the two graphs at right, filled circle markers indicate resistivity profiles through SEI, while unfilled circle markers indicate uncycled samples/regions.

AFM results showed that SEI formation on the cycled 3.2-nm SiO_2 displayed a morphology consistent with SEI formed on native SiO_x. Moreover, optical microscope images showed similar surfaces at the micrometer scale. In contrast, the cycled 5.2-nm SiO_2 sample showed a mostly pristine surface, with no evidence of SEI formation in optical microscope and AFM images. However, on this sample, small occurrences of "ring" structures were identified. Further analysis using SSRM identified these zones as sites of lithiation/delithiation and SEI formation.

Last quarter, investigation into the evolution of SEI through initial stages of cycling (1, 10, and 50 cycles) revealed that the resistivity of Si increases due to extensive lithiation and delithiation of the active material,

likely due to the expansion and contraction that amorphizes the Si structure and disrupts bonds between atoms. Diffusion of species contained in the electrolyte, e.g., F, may also be responsible for this change in the electronic properties of the underlying Si. On the cycled SiO_2 samples, uncycled regions of SiO_2 on Si were identified by their low resistivity compared to cycled regions. On the cycled 3.2-nm SiO_2 sample, the entire central region of the wafer appeared to cycle uniformly, with only the outer corners inactive (excluded from electrolyte contact by the O-ring in the cell). SSRM profiles at the inactive edge showed a thickness consistent with ellipsometry measurement of total original film thickness; moreover, the low resistivity of the Si in these regions indicated that no cycling had taken place. On the cycled 5.2-nm SiO_2 sample, there was no noticeable interface left behind by the cell O-ring, suggesting that most of the surface was not subjected to lithiation/delithiation. When viewed in an optical microscope, small "ring" features (20–100 μm in diameter) were revealed on the surface; these domains represent a small fraction of the total surface (<1%). SSRM profiles on uniform central regions showed a thickness consistent with ellipsometry measurement of total original film thickness; resistivity of the Si was also low for these regions, indicating that the electronic properties of the pristine Si were preserved. Within these "ring" features, SSRM resistivity vs. depth profiles revealed a high resistivity of Si consistent with substantial cycling, showing thickness greater than the original 5.2-nm SiO_2 film.

Comparison of the SEIs formed uniformly on native SiO_x and 3.2-nm SiO_2, and nonuniformly on 5.2-nm SiO_2 reveals significant differences in thickness and electronic resistivity, indicating that their composition may also differ. SEI formed on native SiO_x shows a much greater thickness, featuring a relatively low-resistivity layer between a highly resistive surface layer and the underlying Si. SEI formed on both thermally grown SiO_2 samples was significantly thinner and appeared to be absent the relatively low-resistivity layer present in the SEI formed on native SiO_x. If resistivity measurements of the underlying Si layer indicate an equivalent amount of lithiation and delithiation between the three samples presented, then the SEI formed on the thicker thermally grown SiO_2 may be less prone to continual growth when compared to SEI formed on native SiO_x. A comparison of all the AFM and SSRM results are listed in Table 1.

Table 1. SEI Formation on Model Si Surfaces

	Native SiO_x	3.2-nm SiO_2	5.2-nm SiO_2
Homogeneity	Uniform	Uniform	Highly nonuniform *(only within ring structures)*
Thickness	Thicker	Thin	Thin
Surface Morphology	Relatively rough SEI surface morphology	Relatively rough SEI surface morphology	Smooth SEI surface morphology
Resistivity of SEI	Resistive surface layer, low-resitivity interior layer	Resistive throughout	Resistive throughout
Resistivity of Underlying Si	Higher within uniform lithiation area	Higher within uniform lithiation area	Higher within ring structures, equivalent to pristine Si elsewhere

Conclusions

Characterization with optical microscopy, AFM, and SSRM showed that uniform lithiation, delithiation, and SEI formation occurs for native SiO_x and for thinner SiO_2 oxide (< 5 nm) films. On thicker SiO_2 oxide films, lithiation occurs nonuniformly in small (20–100 μm diameter) regions that present as "rings" in the microscope. SEI formed on native SiO_x is comparatively thicker and features an inner layer of relatively low-resistivity material. The electronic resistivity of the underlying Si increased significantly due to lithiation/delithiation reactions.

Electrochemical Testing of Silicon Wafer Anodes with SiO$_2$ Coatings (NREL)

Manuel Schnabel (NREL), Paul Stradins (NREL)

Background

Polished silicon wafers provide the most controlled silicon material with which to study the fundamental processes occurring during the lithiation of silicon from an electrolyte. In addition, they can be oxidized, resulting in dense SiO$_2$ layers of varying thickness whose effect on lithiation and battery electrochemistry can be studied as a model system for—typically oxidized—Si powders that would be used in commercially relevant batteries. In the following, we describe results obtained on Si wafer anodes with 1.3–5.0-nm SiO$_2$ coatings, prepared by thermally growing SiO$_2$ of the desired thickness on Si in an N$_2$:O$_2$ ambient at 850°C. The anodes were characterized in half-cells using the O-ring cells presented last quarter, which restrict the electrochemically active area to the oxidized front surface of the wafer and eliminate edge effects.

Results

Using these O-ring cells, we proceeded to study the effect of 1.4–5.2-nm thermal SiO$_2$ coatings on the lithiation of Si wafers. Galvanostatic cycling was performed at 20 µAcm^{-2} in Gen2 electrolyte against Li metal counter and reference electrodes with no lower-voltage cutoff; the results are summarized in Fig. 1. From the electrochemical data, it can be seen that there is a stark difference between samples with less than 3.0-nm SiO$_2$ and more than 3.0-nm SiO$_2$.

Samples with less than 3.0-nm SiO$_2$ all cycle in the same manner: their cycling curves overlap (except for the very start, where 2.1-nm and 2.6-nm SiO$_2$ samples exhibit a spike to negative voltage vs Li (V$_{Li}$), whereas the 1.4-nm sample does not); their coulombic efficiencies overlap at over 99% from the 2nd cycle onwards, and photographs of cycled samples indicate uniform lithiation.
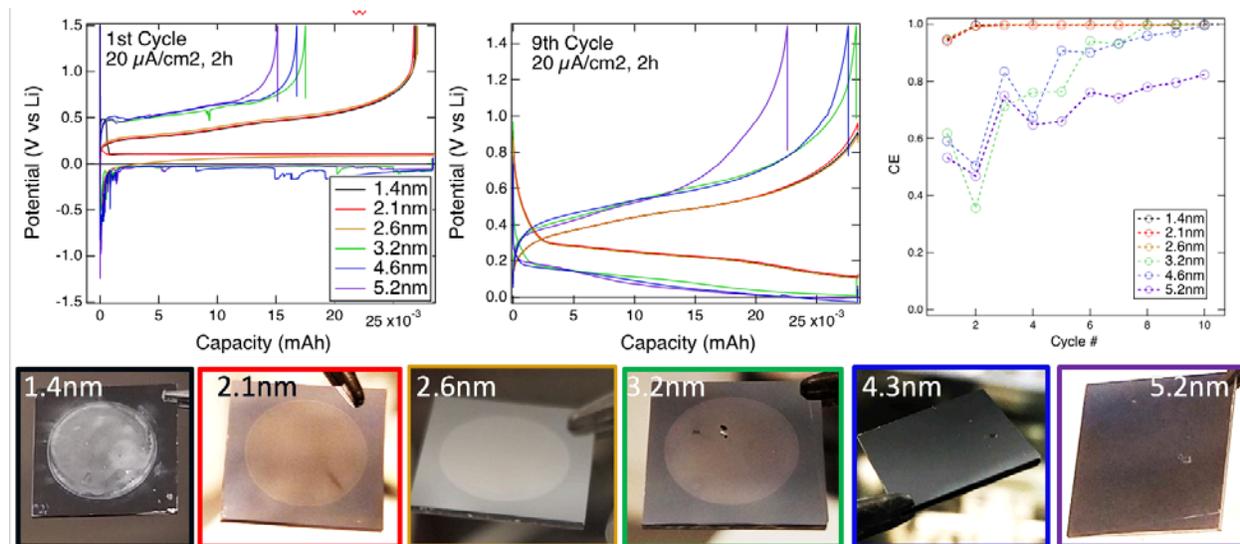
Figure 1. Cycling of Si wafer anodes with variation of SiO$_2$ coating thickness at 20 µAcm^{-2} with no lower-voltage cutoff. Top: 1st and 9th cycles as a function of SiO$_2$ thickness (left, middle), and coulombic efficiency as a function of cycle number (right). Bottom: Photographs of Si wafers after 10 cycles.

In contrast, samples with more than 3.0-nm SiO$_2$ initially only lithiate at negative voltages vs Li, exhibit low coulombic efficiencies, and photographs of cycled samples show only localized lithiation or Li plating. However, by the 9th cycle, they exhibit markedly higher coulombic efficiency, and cycling occurs at positive

V_{Li}, although the difference between lithiation and delithiation voltages is higher than for thinner oxides, indicating that a higher resistance remains.

Nevertheless, it appears that samples with more than 3.0-nm SiO_2 undergo a change within the first 10 cycles that facilitates lithiation, allowing it to occur at positive V_{Li} and higher coulombic efficiency. To determine whether this is due to prolonged exposure to low V_{Li}, we acquired a second dataset on sister samples by holding them at 0.01 V_{Li} and recording the current; these data, along with images of tested anodes, are shown in Fig. 2.
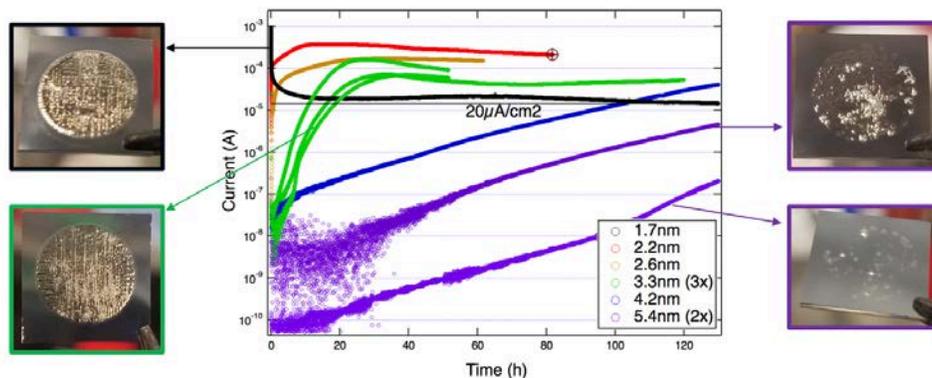
Figure 2. Chronoamperometry at 0.01 V_{Li} for different SiO_2 thicknesses. Photographs of selected samples at the end of testing are shown.

Two regimes are apparent: samples with <3.0-nm SiO_2, which all cycled identically, rapidly reach currents above the 20 μAcm^{-2} previously used for cycling and reach a steady-state lithiation current after 15–20 h. Examination of the anodes after testing reveals uniform lithiation overlaid with cracks resulting from the long duration of lithiation. On the other hand, samples with more than 4.0-nm SiO_2 initially exhibit very low currents, which rise slowly and exponentially by 2–3 orders of magnitude. This process appears to proceed at a fixed rate (the slopes of the corresponding curves are very similar), but the starting current varies widely, even among two nominally identical samples with 5.4-nm SiO_2. Examination of these two anodes shows that lithiation or Li plating in this regime is highly nonuniform: the process initiates at pinholes, and then spreads radially. The somewhat random pinhole density on a given sample appears to be responsible for the initial current, from which the increase in current with time proceeds. The transition between the two regimes appears to occur around 3-nm SiO_2; hence, three samples with 3.3-nm SiO_2 exhibit intermediate behavior.

Conclusions

We have used O-ring cells to study the lithiation of SiO_2-coated Si wafer anodes. A strong dependence of lithiation on SiO_2 thickness is observed in both cycling and chronoamperometric measurements. Below 3.0-nm SiO_2, lithiation upon cycling is homogeneous and occurs with high coulombic efficiency, and holding at 0.01 V_{Li} leads to a rapid current rise that reaches steady-state in under 24 h, ultimately yielding uniform lithiation and cracking. Conversely, above 4.0-nm SiO_2, initial lithiation upon both cycling and holding at 0.01 V_{Li} is very inhomogeneous, occurring at pinholes first and then spreading radially, decreasing the resistance to further lithiation as the process proceeds.

Chemical Reactivity and Resulting Structure of Lithium Silicates

Gabriel Veith, Brenda Smith, and Rebecca McAuliffe (ORNL)

Background

We have been pursuing a set of questions revolving around the formation and reactivity of lithium silicates. In this work, we synthesized high-purity raw silicates through the direct reaction with Li_2CO_3 and SiO_2 to form Li_2SiO_3, $Li_2Si_2O_5$, and Li_4SiO_4. The as-prepared materials were loaded in a glovebox and subjected to a 500°C anneal for 2 hours to remove water and any surface carbonates. The dried materials were ground to a velvet-like consistency in the glovebox prior to use. One gram of the resulting materials was exposed to 5 mL of the standard 1.2M $LiPF_6$ 3:7 wt% ethylene carbonate/ethyl methyl carbonate at 60°C for 72 hours to explore the reactivity of crystalline Li-Si-O materials with the electrolyte. Previous work on amorphous films indicated that the amorphous films reacted readily with the electrolyte, forming a complex Li-Si-O-P-F layer.

After aging, the powders were collected and washed four times with 15 mL aliquots of dry dimethyl carbonate to remove residual solvents. The samples were dried in vacuum for 24 hours and packed in 3-mm glass capillaries. In addition, reference samples of LiF, Li_2CO_3, ethylene carbonate, $LiPF_6$, and pristine starting materials were loaded in capillary tubes. The samples were analyzed on the Nanoscaled-Ordered Materials Diffractometer (NOMAD) located at the Spallation Neutron Source. This instrument is ideally configured to collect data suitable for pair distribution analysis, which is useful for identifying structural correlations within amorphous material. Furthermore, neutrons are especially sensitive to low Z elements such as Li and O, allowing for structural determination of materials containing these elements.

Results

After exposure to the electrolytes, the resulting materials were still white, with no evidence of discoloration. The materials were analyzed using X-ray photoelectron spectroscopy, infrared spectroscopy, and neutron scattering. The XPS data show clear evidence for residual surface species. The fluorine content was extremely low (about 5 at%) whereas C-O species attributed to about 60% of the total surface chemistry; see Figure 1. Analysis of the data revealed the F was predominately PF_6^- species that was not removed during the DMC washing step. The carbon and oxygen was prediminately C-O species from the electrolyte. It should be noted that the surface layer was thinner than 10 nm because the Si from the Li_4SiO_4 was still visible in the spectra.
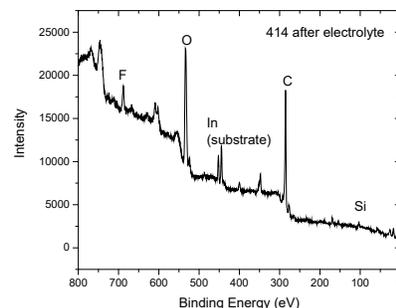
Figure 1. Representative XPS data collected for the Li_4SiO_4 sample after electrolyte exposure.
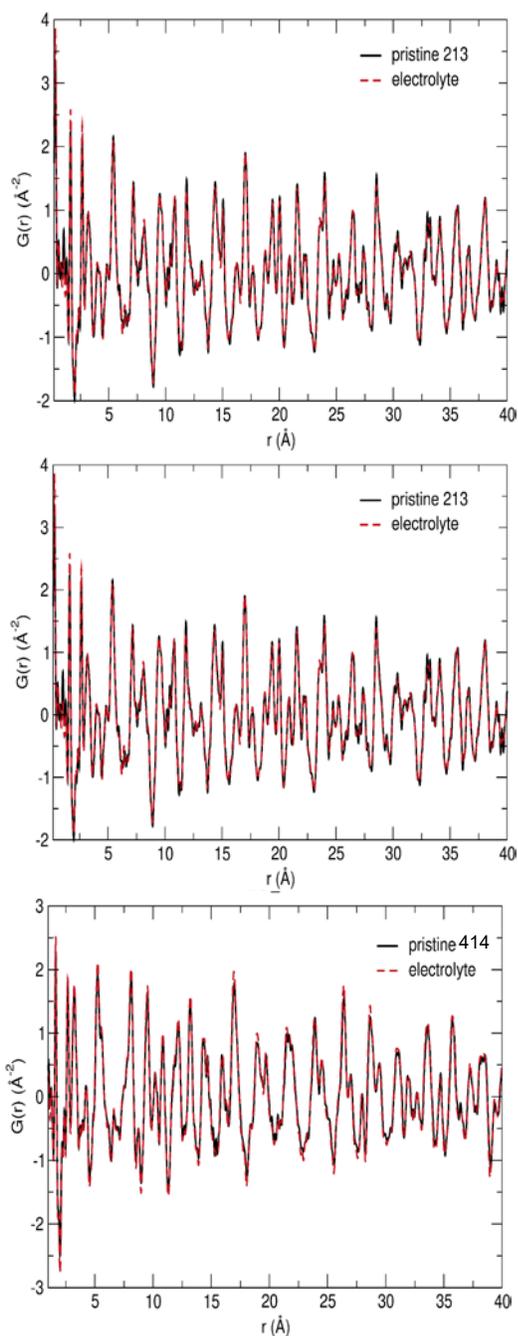
Figure 2. Neutron PDF data collected for Li_2SiO_3 (top), $Li_2Si_2O_5$ (middle), and Li_4SiO_4 (bottom) for the raw material (black line) and material exposed to electrolyte (red dashed line).

The neutron PDF data collected for these samples are shown in Figure 2. The black lines are the data collected for the pristine samples and the red dashed line shows the data after electrolyte exposure. From these data, there is no evidence of changes to the bulk structure of the Li-Si-O materials. Furthermore, there is no evidence of the formation of an amorphous surface phase on the crystalline materials. If there was such an amorphous phase, we would see new peaks and valleys in the data. Finally, there was no evidence for significant concentrations of organic species in or on the sample, which would attenuate the neutron signal due the the absorption of neutrons by H.

Together, this indicates that the crystalline Li-Si-O are very stable against the electrolyte. This is true at high temperatures where one would expect greater reactivity. Furthermore, we see no evidence of other significant lithium or organic phases trapped on the surface. These data do not exclude catalytic activity of the materials but does point to stability in the crystalline phase. This is in contrast to the data measured for amorphous materials reported previously, which demonstrated significant electrolyte reactivity.

Conclusions

In summary, we have explored the synthesis of crystalline Li-Si-O phases and demonstrated them to be robust against electrolyte reactivity at elevated temperatures. The crystal structures remain intact during the reactivity indicating that the Li in the lattice is trapped, which would be consistent with their low ionic conductivity.

Understanding and Design of the Si SEI from Coupled Molecular Dynamics – First-Principles Calculations (UC Berkeley)

Kristin Persson, Sang-Won Park, Tingzheng Hou (UC Berkeley)

Background

The Gen2 electrolyte exhibits superior performance compared to the conventional ethylene carbonate (EC) electrolyte for Si anode systems. Based on our previous simulation on EC electrolyte systems, we continued our work to investigate the solvation structure of Gen2 electrolyte and the influence of fluoroethylene carbonate (FEC)through classical molecular dynamics (MD) simulations. The degree of ionization at the silica surface varies depending on the environment in the electrolyte, affecting SEI formation by changing the electric potential and Li^+ ion distribution at the surface. The dependence of the silica surface configuration on the electric potential is investigated.

Results
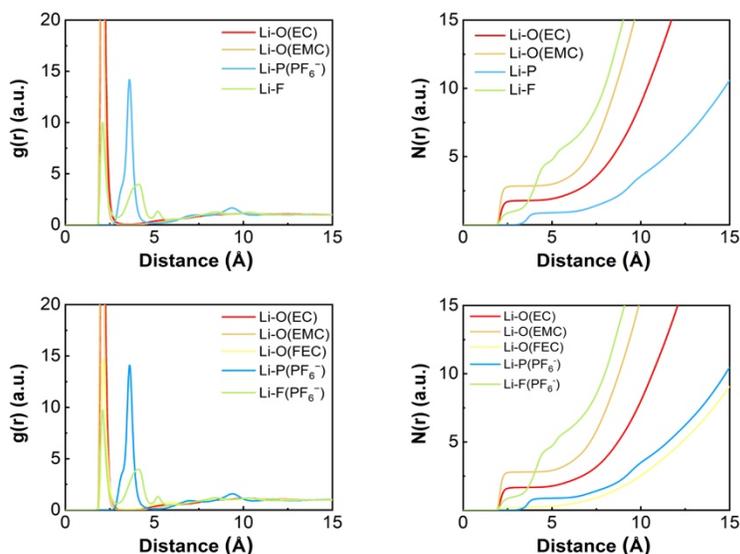
Figure 1. Calculated radial distribution functions g(r) and the corresponding integrals N(r) of Li-O(EC), Li-O(EMC), Li-P(PF_6^-), and Li-F(PF_6^-) pairs of (a) (b) Gen2 electrolyte, and Li-O(EC), Li-O(EMC), Li-O(FEC), Li-P(PF_6^-), and Li-F(PF_6^-) pairs of (c) (d) Gen2 electrolyte with 10%mol FEC additive.

A set of simulations for Gen2 electrolyte (1.2 M $LiPF_6$ in EC:EMC 3:7) with or without 10% FEC was conducted to investigate the solvation structure of Gen2 electrolytes and the influence of FEC additive. The radial distribution function g(r) and the corresponding integrals N(r) of Li-X (X = O(EC), O(EMC), P(PF_6^-), Li, F(PF_6^-) for Gen2 and X = O(EC), O(EMC), O(FEC), P(PF_6^-), F(PF_6^-) for Gen2 w/ FEC) pairs are summarized in Figure 1. The large peak (compared with previous EC electrolyte) of the Li-F pair at ~2 Å shown in Figure 1a suggests that for Gen2 electrolytes, a significant amount of $LiPF_6$ salt forms contact ion pairs (CIP) or aggregates (AGG), while the solvent-separated ion pairs (SSIP) present as minority species. By integrating the g(r) to 3.0 Å, the total coordination number (CN) of Li ion for Gen2 is obtained and compared with previous results of EC electrolyte, as shown in Figure 2. With EMC as majority of the solvent, the first solvation shell of Gen2 electrolyte is occupied by 2.8 EMC and 1.7 EC, which is consistent with intuition. However, as depicted in Figure 1, the Li^+ solvation sheaths present an average of 0.88 PF_6^- anions, indicating that, on average, most of the Li cations are coordinated with PF_6^- anions. This could be attributed to the decrease of solvent dielectric constant, which needs more future verification and comparison to available experiments.
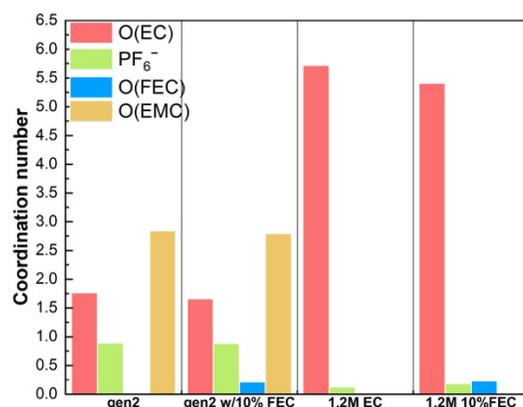
Figure 2. (a) The calculated total coordination number for Li$^+$ in Gen2 electrolyte with or without 10% FEC and 1.2 M LiPF$_6$ in EC with or without 10% FEC with specifications of the contributions from EC, FEC, and PF$_6^-$, and EMC.

Upon addition of 10% FEC into the Gen2 electrolyte, the solvation structure is altered in the same way as EC electrolyte. FEC, as a new solvating agent, appears in the first solvation shell with a coordination number of 0.21, which agrees well with our previous simplified EC electrolyte model (0.23). Meanwhile, the CIP ratio remains the same for Gen2 electrolyte after adding FEC, which could be explained by the intermediate solvating ability of FEC between EC and EMC. EC electrolytes are known to promote salt dissociation due to its high dielectric constant (ε = 90), as well as donor number. FEC exhibits a slightly lower dielectric constant (ε = 78.4). In contrast, EMC has the lowest dielectric constant (ε = 2.96), which results in less dissociation of LiPF$_6$ and weakened donor ability (i.e., smaller CN of Li+ solvent).

While the bulk solvation structure provides a measure of the equilibrium electrolyte properties, we expect interaction with the interface to perturb the equilibrium solvation structure. As previously reported, different Li+ coordination and solvation structures give rise to different reduction behavior, and hence, influence the formation of the SEI. For example, we expect a higher density of Li-PF$_6$ contact ion pairs to promote SEI formation involving LiF. To study the liquid structure at the silica surface, we used both crystalline (α-cristobalite ($10\bar{1}$)) and amorphous silica with fully protonated dangling bonds, which is constructed by the INTERFACE force field [1], and conducted by classical MD simulations. Silica surfaces are known to exhibit various values of "point of zero charge" (PZC) or isoelectric point (IEP) under different conditions, ranging from 1.6 to 6.3 [2]. Here, we study general trends of the electrical properties of a silica surface in 1 M LiPF$_6$/EC by changing the surface condition of the silica—crystalline to amorphous—and increasing the degree of ionization of the surface silanol groups (Figure 3). The ionized silica surface is modeled by removing protons from the dangling Si-OH bonds, and the negatively charged surface is simulated to study the charge effect with the possible hydrogen bonds between Si-OH and electrolyte molecules.
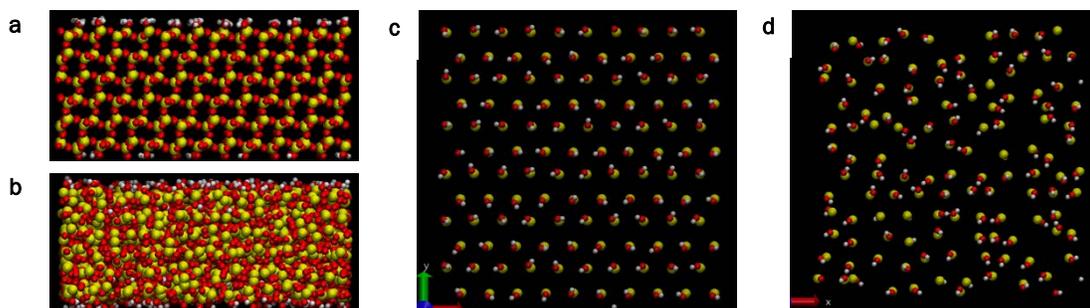
Figure 3. (**a-b**) Snapshots of slabs of crystalline (**a**) and amorphous (**b**) silica with fully protonated dangling bonds: the dimension of the slab is 50.83×52.37×23.61 Å^3 (**c-d**) Snapshots of the surfaces of crystalline (**c**) and amorphous (**d**) silica. Dangling bonds are substituted with silanol groups. Area density of silanol groups is set to 4.7 nm^{-2}, and degree of ionization is varied from 0 to ~0.9 nm^{-2}, which is equivalent to 20% of surface silanol groups.

Distribution of ions and the contact ion pairs (CIPs) at the silica surface are investigated (Figure 4), defining the interfacial region as within 3 Å from the silanol oxygen atoms at the surface. The density of Li$^+$ ions at the interface (Figure 4a) increases with surface ionization, where amorphous silica shows less dependence of the density of Li$^+$ on the ionization at the interface than the crystalline. The density of CIPs (Figure 4b) at the crystalline surface shows non-monotonous behavior with ionization: the amorphous silica favors more ion pairs at the interface than the crystalline silica in the 0% ionization case. Si and O are exposed to the electrolyte region in the amorphous silica whereas they are covered with protons in the regular silica, as seen from the snapshots in Figure 3. The exposed O atoms of the 0% amorphous silica bring the Li$^+$ ions to the surface; thus, there is more probability of ion pairing at the amorphous surface. Our simulation suggests that a slightly ionized (<10%), or negative crystalline silica surface induces more ion pairs.
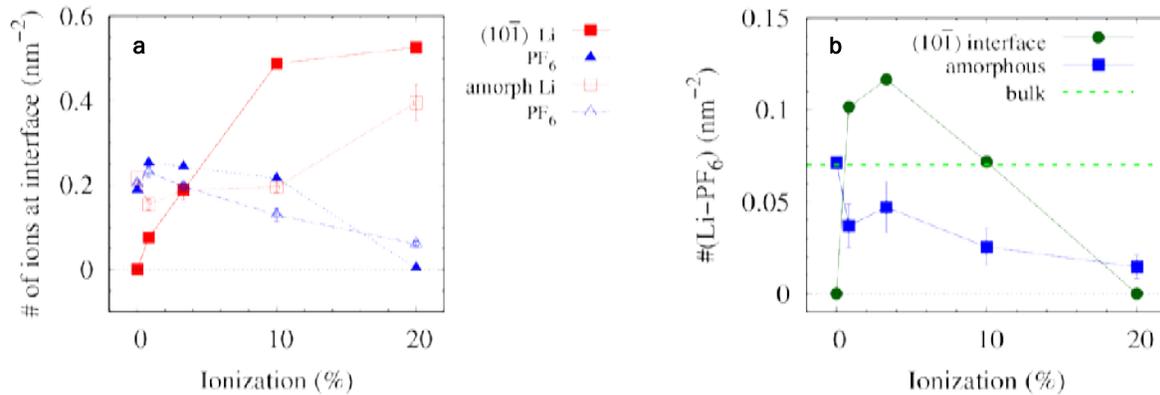
Figure 4. Distribution of Li$^+$ ions (**a**) and density of contact ion pairs (Li-PF$_6$) (**b**) at the surfaces.
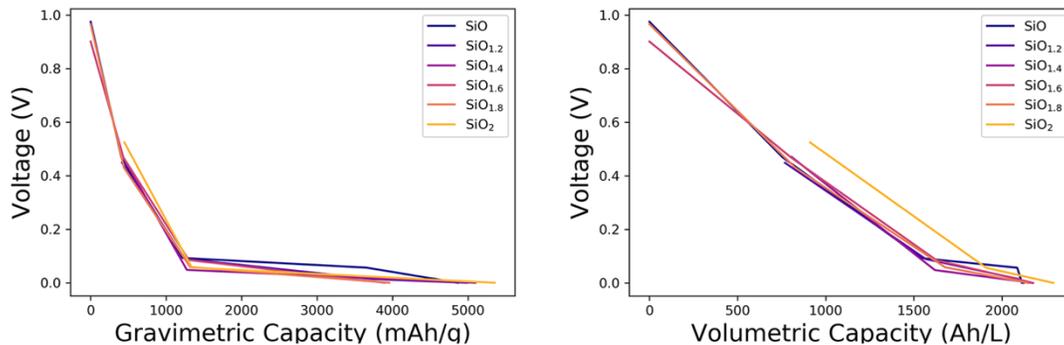
Figure 5. Equilibrium voltage profiles of SiOx plotted vs a) gravimetric capacity (with respect to the starting electrode weight) and b) volumetric capacity

The oxide layer of Si is known to be amorphous and its thickness tunable, but the composition of the native oxide layer of Si can vary with processing and film thickness. The composition can play a large role in the lithiation behavior of the electrode in a Li-ion battery cell. Here, we study the effects of sub-stoichiometry by studying the lithiation behavior of various sub-stoichiometric compositions of a-SiO$_x$, for x={1, 1.2, 1.4, 1.6, 1.8, 2}. We use AIMD and first-principles calculations to generate amorphous structures, as discussed in previous reports. When examining the equilibrium voltage profiles of the amorphous SiO$_x$ phases, given in

Fig. 5, we observe that SiO_x all lithiate at similar potentials, although with differing gravimetric capacity due to the differing weights of the starting electrode material. The voltage profile vs volumetric capacity are similar, with similar overall volumetric capacities, due to the parity in the density of the fully lithiated states.

Conclusions

1. Our preliminary MD simulations show that the Gen2 electrolyte exhibits significantly higher CIP ratio than the pure EC electrolyte. When 10% FEC is added, the Li+-FEC pair exhibits a similar coordination number (~0.2) as EC electrolyte, which supports our previous finding that FEC alters the composition of the first solvation shell and thus influences the reduction potential of the electrolyte.
2. Crystalline and amorphous silica models were developed with a varying degree of protonated surface. Our simulation suggests that a slightly ionized (<10%) or negative crystalline silica surface induces more ion pairs at the interface.
3. We find in our AIMD and first-principles study of SiOx, for $1 < x < 2$, that the compositional variance of O has little impact on the lithiation of the native oxide film with regard to lithiation mechanism and lithiation voltage.

References

[1] F. S. Emami, P. Valeria, R. J. Berry, V. Varshney, S. V. Patwardhan, C. C. Perry, H. Heinz, Force Field and a Surface Model Database for Silica to Simulate Interfacial Properties in Atomic Resolution, *Chem. of Mater.* 26, (2014) 2647–2658.
[2] M. Kosmulski, pH-Dependent Surface Charging and Points of Zero Charge. IV. Update and New Approach, *J. Colloid Interface Sci.* 337 (2009): 439–48.

Oxygen Effect on Passivation Bbehavior of Silicon Electrolyte Interface

Yun Xu, Andriy Zakutayev (NREL)

Background

Oxygen content in silicon is a large variance in the SEISta project. Oxygen content not only affects the lithiation mechanism, but also affects the surface SEI formation and stabilization. In this quarter, we studied the SiOx film with different O content.

Results

Thin film with different O content was deposited by the following method: 1) Si thin film was sputtered in pure Ar; 2) SiOx with low O content was sputtered with O_2 gas introduced for process gas; and 3) SiOx film with higher O content was sputtered with Si and SiO_2 targets. The three films are labeled as 1) Si; 2) SiOx; and 3) Si+SiO_2. The films were assembled into a coin cell and tested with the protocol: galvano discharge with 5 µA, hold at 50 mV until $5e^{-7}A$ current is reached, which is a reasonable value to consider as passivated. Holding voltage at 50 mV for 24 h gave noisy data because it is beyond the measurement accuracy.

Figure 1a shows the 1-cycle charge and discharge profile of the three films. Clear differences can be seen when O is introduced in the film. Silicon thin film gets lithiated below 0.25 V, but the SiOx film shows a larger slope for the discharge curve, mainly because of the random mixture of Si and O atoms. The difference at the high voltage range above 0.5 V originated mainly from the conversion reaction

$$SiOx + (2y+4z)Li^+ + (2y+4z)e^- \rightarrow (1-y)Si + yLi_2O + zLi_4SiO_4 \dots\dots\dots\dots\dots\dots(1)$$
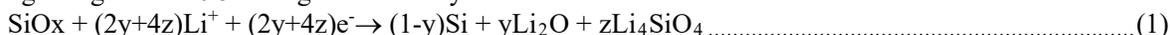
Li_2O and Li_4SiO_4 are not reversible products. However, they are considered to be the buffer materials to alleviate the volume-expansion problem for silicon. The buffer effect is not discussed in this report. DQ/DV from the 1st discharge is plotted in Figure 1. There are several peaks between 0.4 V and 0.8 V; the peak around 0.7 V is the reduction of electrolyte. Peaks at 0.5 V (Si+SiO_2) and 0.6 V (SiOx) are identified as the conversion reaction (1). These reactions are not reversible as seen from the second cycle. The voltage profiles from the 1st and 2nd cycles of each film are displayed in Figure 2a, b, and c. DQ/DV from the second cycle is shown in Figure 2d. From the second cycle, it can be seen that all the films exhibit the same lithiation peaks of Si. Peaks at 0.5 V and 0.6 V are gone from the second cycle.
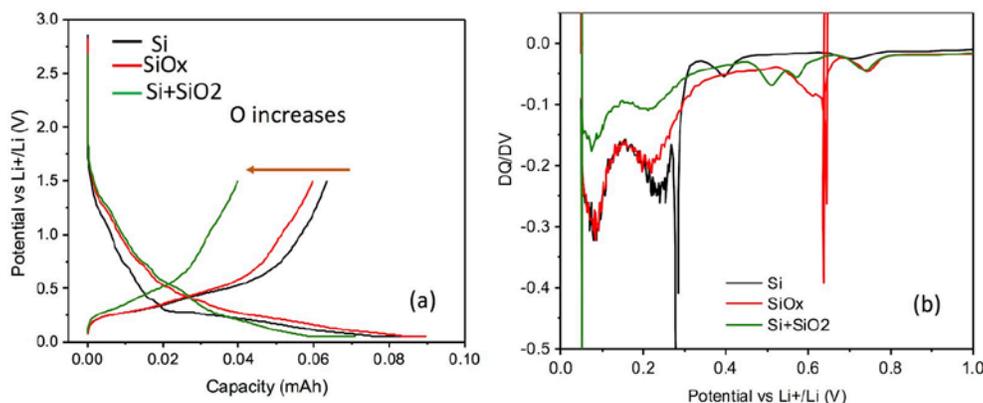
Figure 1. a) Voltage profiles of the three films; b) DQ/DV from the 1st discharge profiles.
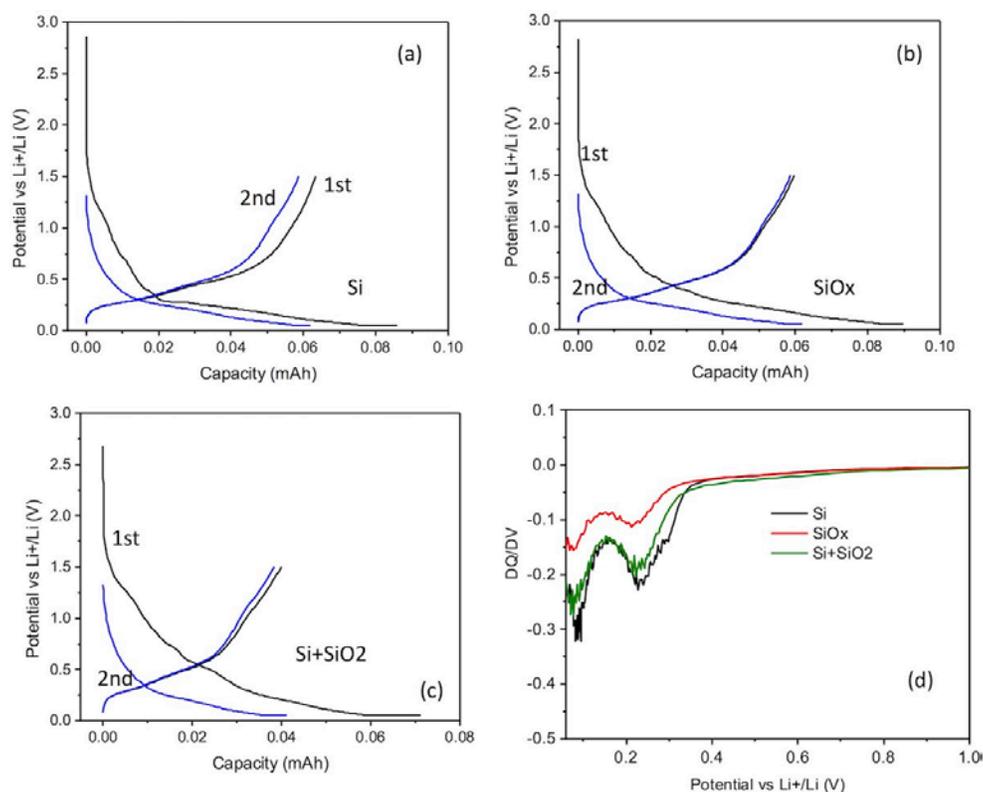
Figure 2. a) DQ/DV profiles for the 1st discharge; b) DQ/DV profiles for the 2nd discharge

The O effect on the SEI stabilization was checked by looking at the parasitic currents at 50 mV. Instead of looking at the residue current, we looked at the time to reach a cutoff current of $5e^{-7}$ A. Compared to three films, SiOx, which has O but less O compared to <Si+SiO$_2$>, shows the least parasitic reaction because it took the least time to reach the cutoff current. One of the possible reasons is the conversion reaction of SiOx to Li$_2$O, and Li$_4$SiO$_4$ could help the stabilization of SEI, while too much conversion reaction is driving Columbic efficiency low.
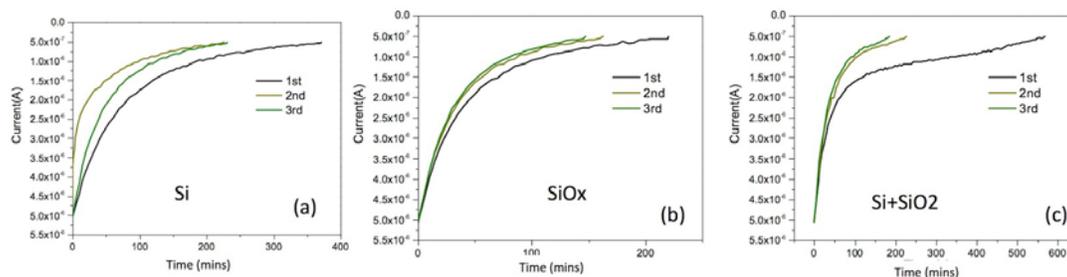
Figure 3. Current-time plots of a) silicon thin film; b) SiOx thin film; c) Si+SiO$_2$ film.

Conclusions

Thin films with different O contents were studied in this quarter. As we increased the O amount into the film, first-cycle coulombic efficiency decreased because more conversion reactions occurred during the 1st cycle. However, little O is shown to help the stabilization of SEI because of the conversion reaction from SiOx. Too much O film is shown to decrease coulombic efficiency significantly due to irreversible conversion reaction, as well. Further analysis is necessary to see what the conversion reaction products are, and why it helps the SEI. Quantitative analysis of the O level in the film is also ongoing.

Part 2. SEI Stability

Silicon Electrolyte Interface Stabilization (SEISta) [LBNL]

S. Jurng, I. Hasa, P. Ross, R. Kostecki

Background

The primary objective of our effort is to clarify and understand the processes occurring at the silicon/electrolyte interface. The reductive decomposition of the electrolyte in lithium-ion systems employing silicon anodes is inevitable because the working potential of the electrode is far below the electrochemical stability window of the electrolyte components. In principle, the insoluble decomposition products precipitating on the electrode surface result in the formation of a passivating surface film that suppresses further electrolyte decomposition.[1,2] However, the inherent instability of the silicon/electrolyte interface strongly inhibits the surface passivation, which is further endangered by the mechanical instability of the electrodes—which, upon alloying with lithium, experience a huge volume expansion responsible for active material cracking and consequential instability of the passivating film.[3] A better understanding of the kinetic processes occurring upon cycling will enable an efficient implementation of silicon-based electrodes in high-performance lithium-ion batteries. To accomplish this, we address the inherent non-passivating behavior of silicon model electrodes in organic electrolytes. In particular, this last quarter, we have been focused on the "Corrosion Task" of the SEISta project, which is a coordinated research thrust aiming at the understanding and evaluation of the non-passivating behavior of silicon anodes. The overall goal of this effort is to provide a basic understanding and ways of effective mitigation of Si anode corrosion in organic carbonate-based electrolytes. Oak Ridge National Laboratory fabricated all the model electrodes for the Corrosion Task, and the team at Lawrence Berkeley National Laboratory electrochemically investigated the corrosion currents involved upon cycling.

Results

In the last quarter, our research efforts have been mainly dedicated to evaluating the passivating properties of silicon anodes. We developed two electrochemical protocols to be employed for determining the corrosion currents in a silicon half-cell configuration. Additionally, a screening study toward defining the best model electrode to be investigated led to the selection of silicon thin films (500-nm Si on copper) with a native oxide layer of about 3 nm as the model electrode of choice.
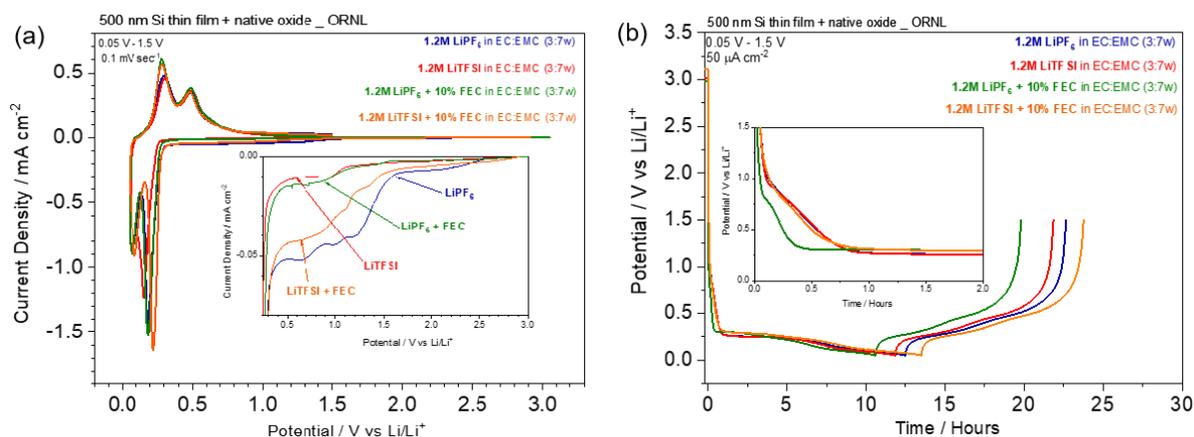
Figure 1. (a) First lithiation–delithiation process of 500-nm Si thin film on Cu foil observed by cyclic voltammetry by using four different electrolyte solutions. A scan rate of 0.1 mV s^{-1} has been applied within the 0.05–1.5 V potential range. Inset shows the enlarged potential region of the electrolyte decomposition. (b) Galvanostatic cycling test of the same systems.

The 500-nm Si thin film has been investigated in four electrolyte solutions, i.e., 1.2 M LiPF$_6$ EC:EMC (3:7 wt%), 1.2 M LiPF$_6$ EC:EMC (3:7 wt%) + 10%wt. FEC, 1.2 M LiTFSI EC:EMC (3:7 wt%), and 1.2 M LiTFSI EC:EMC (3:7 wt%) + 10%wt. FEC. The electrochemical characterization has been performed both in terms of cyclic voltammetry and galvanostatic cycling test as reported in Fig. 1.

The LiPF$_6$-based electrolyte presents the largest reductive current density, whereas the presence of FEC and the substitution of LiPF$_6$ with LiTFSI strongly reduce the current involved in the process. The observation has been confirmed by galvanostatic cycling test as reported in Fig. 1(b). Indeed, the first coulombic efficiency has been calculated to be: 81.4%, 84.3%, 86.5%, and 75.8%, respectively, for the 1.2 M LiPF$_6$ EC:EMC (3:7 wt%), 1.2 M LiPF$_6$ EC:EMC (3:7 wt%) + 10% FEC, 1.2 M LiTFSI EC:EMC (3:7 wt%), and 1.2 M LiTFSI EC:EMC (3:7 wt%) + 10% FEC electrolyte solutions. Protocol 1 (GCPL + CA) has been applied to the above-mentioned system to understand and evaluate the effect of different salts (LiPF$_6$ vs LiTFSI) and the effect of the additive addition (10% wt. FEC) on the passivating properties of silicon.

Figure 2 reports the galvanostatic cycling test (with associated potentiostatic steps) and the *I vs t* curves obtained during the constant voltage step at 0.05 V for the 500-nm Si thin film in three different electrolytes. The analysis has been performed by applying the first protocol developed within the corrosion task (GCPL+CA).
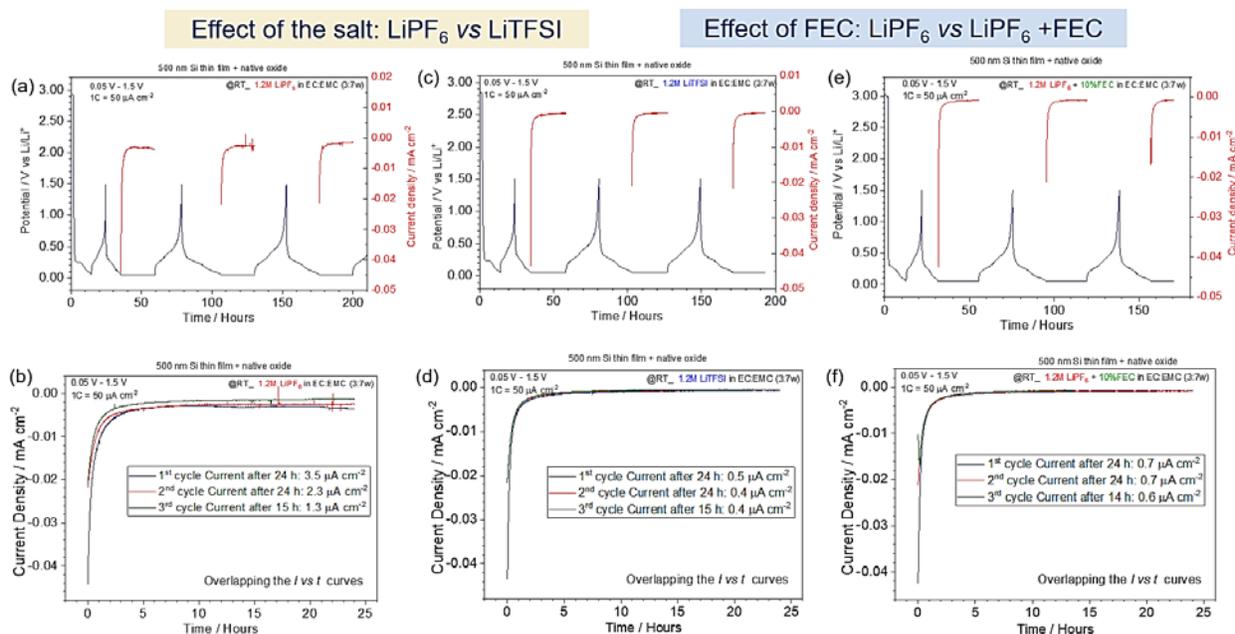
Figure 2. Application of Protocol 1 (GCPL +CA) to the 500-nm Si thin-film model electrode by using (a, b) 1.2 M LiPF$_6$ EC:EMC (3:7 wt%), (c, d) 1.2 M LiPF$_6$ EC:EMC (3:7 wt%) + 10% FEC, and (e, f) 1.2 M LiTFSI EC:EMC (3:7 wt%). (a, b, c) show the galvanostatic cycling with associated potentiostatic step at 0.05 V. (b, d, f) reports the related current density measurement during the potentiostatic step.

It is interesting that the residual currents detected after 24 hours at 0.05 V are very large for the 1.2 M LiPF$_6$ EC:EMC (3:7 wt%) electrolyte, whereas by substituting LiPF$_6$ with LiTFSI, the current value is about 7 times smaller. The same effect is observed with the addition of 10% FEC to the bare 1.2 M LiPF$_6$ EC:EMC (3:7 wt%) solution. The data are in agreement with the CV and GCPL tests reported in Fig. 1. It is also observed

that the passivation of silicon improves upon cycling, as demonstrated by the lower current values observed after the third potentiostatic step when compared to the first one.

In this quarter, we investigated the corrosion behavior of silicon electrodes in the full-cell configuration, in addition to the half-cell configuration, by employing LiFePO$_4$ (LFP) as the cathode electrode. The use of LFP, which acts as a source of a limited amount of lithium, enables a direct visualization of the effect of the silicon corrosion and lithium consumption upon cycling. Figures 3 and 4 show the voltage profiles (Fig. 3) and cycling performance (Fig. 4) of LFP/Si cells using three different electrolyte solutions, i.e., 1.2 M LiPF$_6$ EC:EMC (3:7 wt%), 1.2 M LiPF$_6$ EC:EMC (3:7 wt%) + 10%wt. FEC, and 1.2 M LiTFSI EC:EMC (3:7 wt%).
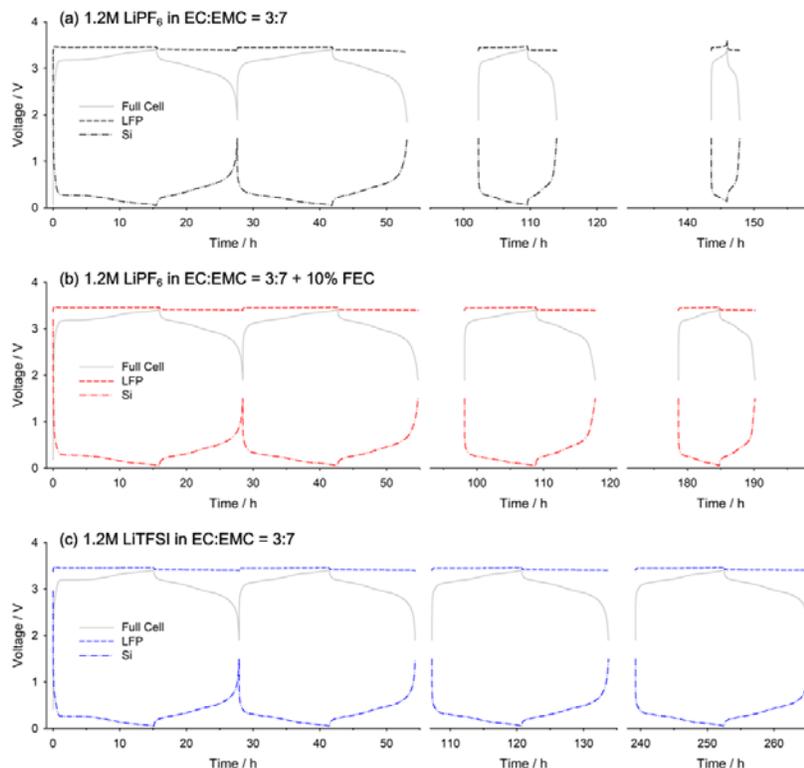
Figure 3. The voltage profiles of LiFePO$_4$/Si cells containing the 500-nm Si thin-film model electrodes (1st, 2nd, 5th, and 10th cycle) with (a) 1.2 M LiPF$_6$ EC:EMC (3:7 wt%), (b) 1.2 M LiPF$_6$ EC:EMC (3:7 wt%) + 10% FEC, and (c) 1.2 M LiTFSI EC:EMC (3:7 wt%).
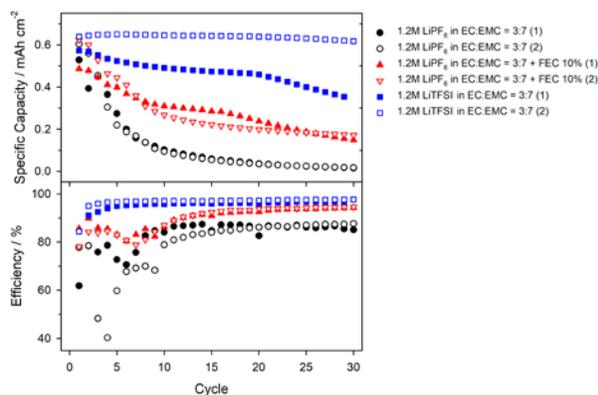
Figure 4. Cycling performance and efficiency of LiFePO$_4$/Si cells containing the 500-nm Si thin-film model electrodes with different electrolyte solutions.

As mentioned above, this full-cell system has a very limited amount of lithium, such that lithium loss upon cycling is directly visible from the remaining capacity of LFP/Si cells. In the initial 10 cycles, the cell with 1.2 M $LiPF_6$ EC:EMC (3:7 wt%) solution lost almost 80% of its initial capacity, which indicates that the lithium consumption from the corrosion behavior on the silicon surface had been very severe. The presence of FEC and the substitution of $LiPF_6$ with LiTFSI improved the cycling performance significantly, comparable to the previous results with the half cells. It should be noted that the cell with 1.2 M LiTFSI EC:EMC (3:7 wt%) presents a remarkably good cycling performance and only loses a marginal amount of lithium upon cycling. These results suggest that the corrosion behavior on silicon affects the performance of full cells such that it needs to be reduced for the commercialization of silicon.

Conclusions

In summary, the non-passivating behavior of silicon thin films has been directly observed for the first time as an independent effect from the cracking of silicon particles due to the lithiation. A visualization of the improvement of the passivation properties upon cycling has been quantified, suggesting a thickening of the passivating film on the silicon surface. The beneficial effect of FEC for the SEI stability has been confirmed in both half- and full-cell configuration. Additionally, the use of LiTFSI as alternative salt to improve the SEI stability is proposed.

Furthermore, we investigated the effect of corrosion of silicon in the full-cell configuration using LFP/Si cells. Due to the non-passivating nature of silicon thin films, the lithium consumption upon cycling was substantial for the standard electrolyte solution. The full-cell results are comparable to our previous observation with the half cells such that the use of FEC and LiTFSI mitigates such silicon corrosion. Furthermore, we are in the process of calculating the lithium loss from such corrosion.

References

[1] E. Peled, *J. Electrochem. Soc.*, **126**, 2047–2051 (1979).

[2] M. Winter, *Zeitschrift Für Phys. Chemie.*, **223**, 1395–1406 (2009).

[3] M.N. Obrovac, V.L. Chevrier, *Chem. Rev.*, **114**, 11444–11502 (2014).

Silicon Electrolyte Interface Stabilization (SEISta)

Jaclyn Coyle (UC Boulder), Kevin Zavadil (SNL), Kyle Fenton, Josey McBrayer, Chris Apblett (SNL)

Background

This quarter, we have focused on characterizing the electrochemistry of the native oxide and "pristine" silicon surfaces by electrochemical cycling for various conditions, starting with either a freshly etched Si surface, or varying amounts of oxide on the surface (either native grown or deposited). These changes can be used to determine if the pristine surface evolves differently than those that have been modified (Q1 milestone). We are also developing new diagnostics (microcalorimetry and stress measurement *in-situ*) to determine how the nature of the silicon surface affects the composition, function, and thickness of the SEI (Q2 milestone).

Results

Cycling Studies (Q1 Milestone)

The performance of 50-nm-grown SiO_2, bare silicon, and native oxide on silicon were studied in 2032 coin cells. The cells cycled at a rate of C/3 between 1.5 V and a minimum of 0.05 V. The lower-voltage cutoff was supplemented by a 5-hour time limit to continue cycling in the event the cells did not reach 0.05 V. The lower voltage was typically ~0.15 V. The electrodes were composed of a degenerately doped silicon wafer with copper on the bottom for electrical contact with a 20-nm titanium adhesion layer, 500-nm copper, and 50-nm silicon thin film on the surface. A new hydrofluoric acid treatment station was set up and used to remove the native oxide of the silicon samples. The capacity and Coulombic efficiency, to date, are shown in Figure 1. Within error, all three sample types performed equivalently. The observed capacities are all above the theoretical capacity achievable at room temperature (3,579 mAh/g). This trend continues past the SEI formation cycles, suggesting that the underlying silicon substrate is being lithiated, in addition to the silicon thin film. This makes the assumed active mass of the electrode incorrect, leading to inaccurate capacities. New electrodes, with silicon thin films on copper foils, are being designed to address this issue.

Because this issue has shown itself across several different experiments at the various laboratories when using a "thick" silicon sample, we are preparing new sample standards for the program that remove this based on the initial work done by Kostecki, where a solid Cu ram was polished, and Si was deposited on the polished surface to a fixed thickness. Although this sample preparation is compatible with the T-cell standards available throughout the program, it is less compatible with the coin-cell standards, and it will not support additional integration into some of the standard test cells being developed for *in-situ* analysis. A new standard sample, based on an evaporated 50-nm Si backed by a 2-µm evaporated Cu foil is being developed, and it should eliminate the issue with anomalous lithiation seen with Si handle substrates.
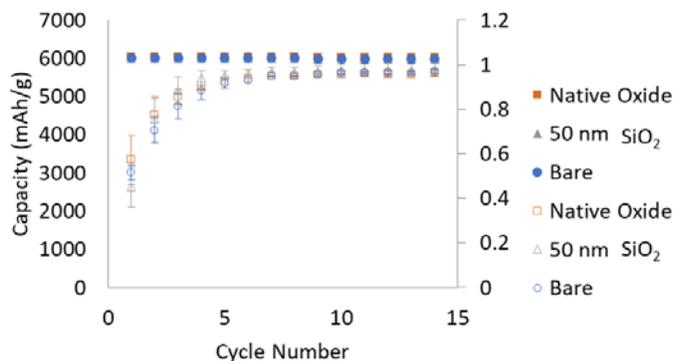
Figure 1. Capacity (solid fill) and coulombic efficiency (outline) for the native oxide (squares), 50-nm SiO_2 (triangles) and bare silicon (circles). The capacities are well above the theoretical room-temperature capacity of silicon. This is attributed to lithiation of the underlying silicon substrate.

Interfacial Stress Measurement for Q2 Milestones

The new electrodes are designed for use in an *in-situ* cell setup for Moiré interferometry. The cell will be used in future measurements of strain in the SEI under varying conditions. The current cell design is shown in Figure 2a, featuring a PEEK body and metal heating block. Two chambers are used to allow for pressure equalization to prevent the thin electrodes from rupturing. The electrodes are 2-µm copper foils with a 50-nm Si thin film, held in place by an O-ring and washer. The thin foil electrodes are intended to enable magnified changes in stress in the electrode, leading to the easier measurement of strain.

For characterization of the electrodes, an Fourier transform infrared (FTIR) spectrometer was obtained and placed in an argon-filled glovebox for future compositional analysis, and a Moiré interferometer was constructed in-house. The first half of the custom microscope is displayed in Figure 2b, including the optical illumination arm, objective, and camera. A schematic of what the finished interferometer will consist of is shown in Figure 2c. The Moiré illumination arm, containing the reference grating, is currently in progress.
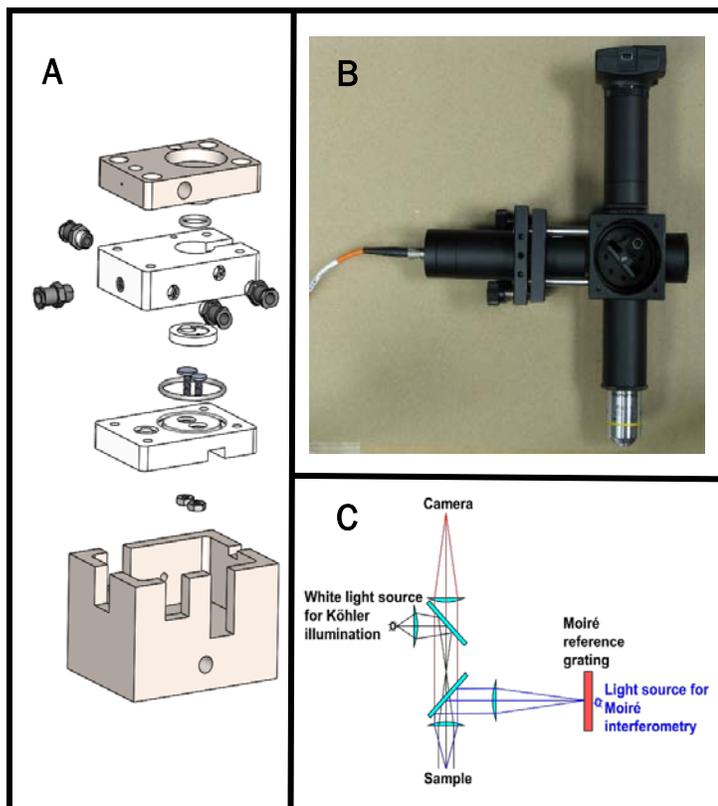
Figure 2. A) Moiré *in situ* cell design with PEEK pieces in white and the metal heating elements in beige. B) Current custom microscope with optical illumination arm complete. C) Schematic of the targeted design of the final Moiré microscope.

Microcalorimetry and Powder Studios

When processed and incorporated into electrodes, silicon active material surfaces are altered from their pristine conditions in a way that likely influences SEI formation and function. To understand the difference between model silicon systems and powders incorporated into electrodes, microcalorimetry has been employed to measure the heat generated from the aqueous processing of silicon powders with LiPAA binders and carbon additives. Based on knowledge of Si surface reactivity and supported by measurement of H_2 gases released during processing, it is assumed that the heat generated during electrode slurry processing is primarily attributable to the reaction of silicon and water to form SiO_2 on the silicon-particle surfaces. Microcalorimetry curves in Figure 3 show the heat flow from a select silicon powder in a slurry mixture over time, as well as fit curves that are used to estimate the total heat generated from the slurries. The energy generated from these

27

slurries is significant, but as shown in Table 1, it still amounts to a relatively small capacity loss of < 4%, even under the extreme case of processing the material for 96 hours. Although data are still preliminary, coin-cell cycling correlates moderately well, showing, for example, an initial Coulombic efficiency (ICE) reduction of 2.67% at 96 hours aging, very close to our predicted value.

Quantification of signal to noise for perfusion testing of silicon and other electrode materials is still underway, with plans to install a fixed-temperature bath and isolated, valved tubing system to reduce sampling noise during liquid perfusion into the microcalorimeter.

Conclusions

Evidence regarding the performance of differing layers of SiO_2 on Si standards seem to show what has been observed by other groups—that the SiO_2 layer thickness does not seem to affect either the capacity or the coulombic efficiency of the cells, which suggests that the SEI oxide layer rides on top of the lithiation and delithiation of the substrate. Given that these are flat samples, it is possible that this layer gives a substantively different response from what would be seen on a particle, in which the increasing internal volume would fracture the oxide and give rise to additional consumption of the electrolyte. Stress measurements to be made will confirm this thinking in the next quarter.
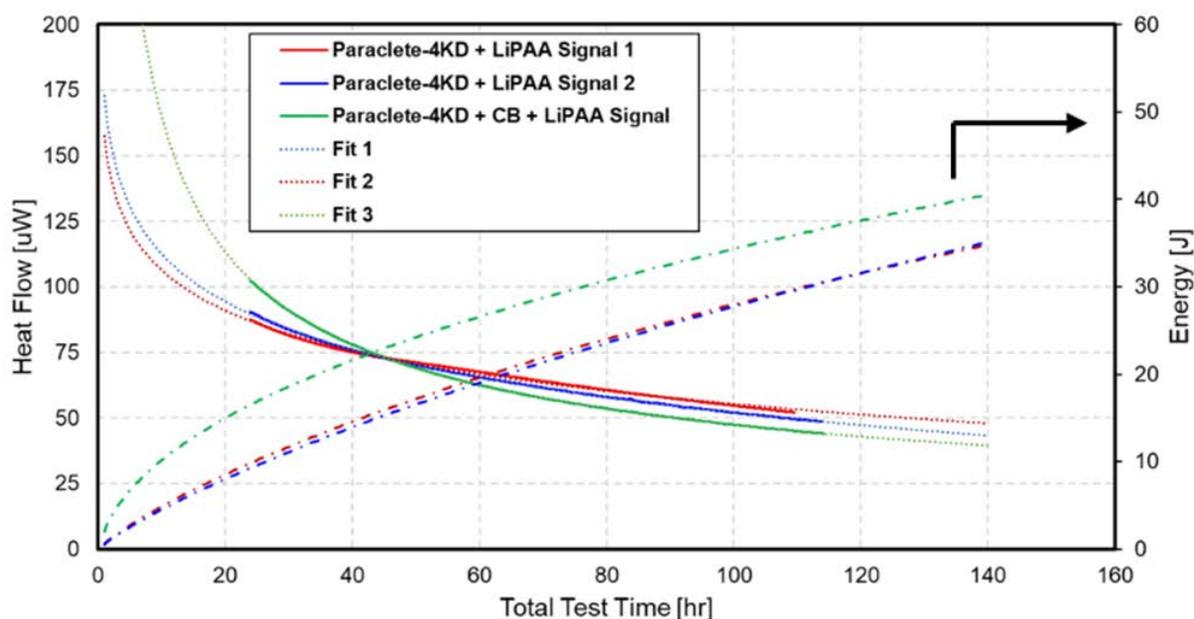
Figure 3. Microcalorimeter heat-flow curves measured for select silicon slurry mixtures along with fit curves to predict the overall degree of reaction in each sample.

Table 1. Quantified energy generation based on the fit curve of the Paraclete-4KD + CB sample in Figure 1 as well as predicted material and performance loss based on the formation of silica

Duration (h)	Energy Generated (J)	SiO₂ Formed (mol)	Silicon Loss (%)	Specific Capacity Retained (%)	ICE Reduction (%)
0	0	0	0	100	0
24	16.522	5.74e-05	0.79	98.31	1.35
48	23.372	9.25e-05	1.13	97.58	1.93
96	33.656	1.17e-04	1.61	96.57	2.73

28

Stability of Glyme-Based Electrolytes for Model Silicon Electrodes: Corrosion and Passivation Studies

Guang Yang , Gabriel Veith, and Jagjit Nanda (ORNL)

Background

The standard Gen2 electrolyte—LiPF$_6$ in an EC/EMC mixture—is widely used for graphite anodes as well for silicon anodes. However, this electrolyte may not passivate silicon as well as it does for standard graphite electrodes. Recent studies by the Lawrence Berkeley National Laboratory (LBNL) team using model a-Si amorphous films show that carbonate-based electrolytes do not passivate the silicon surface during the first few cycles, amounting to a low-level corrosion or side reactions forming an unstable SEI. Based on a suite of characterization methods carried on a model silicon anode (usually with a native nanometer suboxide layer) under the SEISta program, the dominant organic SEI components on a-Si include diethyl alkyl carbonates, carboxylates, and ethers. We hypothesize that solvents built from these components may lead to more stable silicon interfaces. Therefore, the goal of this current work is to investigate ether-based solvents and compatible salts as stable electrolytes for silicon. 50-nm amorphous (a-Si) thin film made at Oak Ridge National Laboratory (ORNL) is used as the model anode. Three electrolytes were evaluated in the current report: Gen2 electrolyte as a benchmark, 1.2M LiPF$_6$ in 1,2-dimethoxyethane (DME), and 1.2M lithium bis(trifluoromethanesulfonyl)imide (LiTFSI).

Results
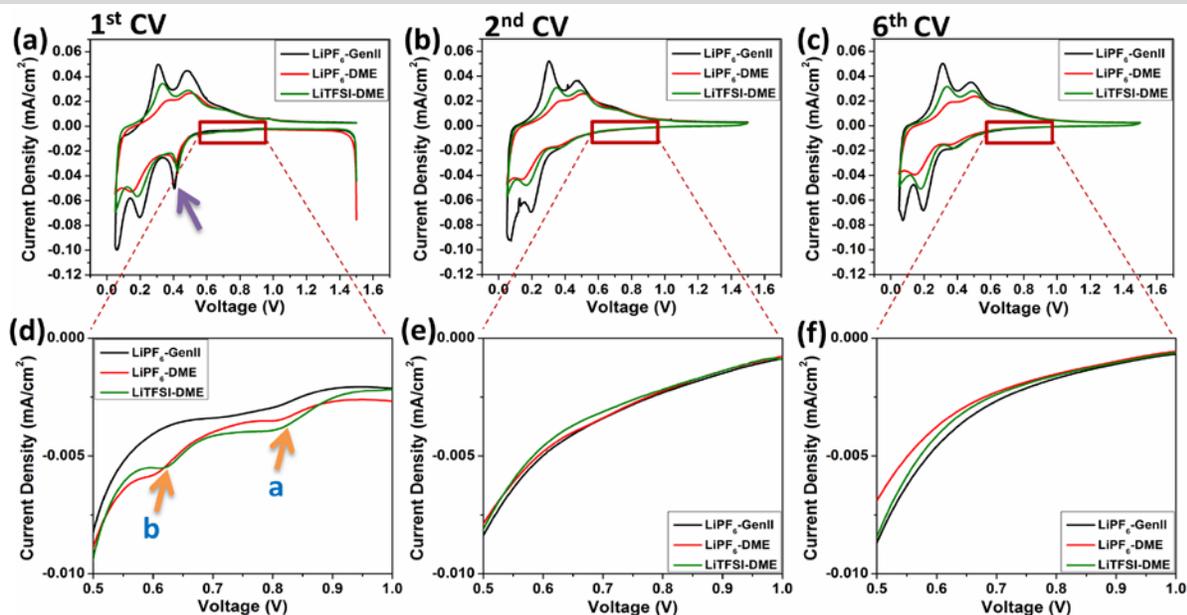
Figure 1. Cyclic voltammograms of a-Si thin0film anodes at different cycles with various electrolytes. (a–c) The overview of the CV plots. (d–f) The magnified view of the CV profile between 0.5 V and 1 V corresponding to (a–c).

The cyclic voltammetry (CV) was measured on the a-Si anode against a lithium counter electrode using different electrolytes at 0.1 mV/s. During the 1st CV cycle, a reduction peak occurs for each of the a-Si samples at around 0.4 V (Fig. 1a, purple arrow). This peak is irreversible as its current-density amplitude deceases notably in the subsequent cycles (Figs. 1b and 1c). Such a peak originates from the initial reaction between Li and pristine a-Si, indicating an irreversible structural change for a-Si.[1] We closely monitored the CV profiles between 0.5 V and 1.0 V for all three electrolyte systems. For the Gen2 electrolyte, a reduction peak occurs at around 0.75 V, ascribed to the EC ring-opening reaction during the initial cycle.[2] Interestingly, the onsite electrolyte reduction for both DME-based electrolytes

29

occurs at higher potentials than for the Gen2 electrolyte (>0.8 V marked by arrow "a" in Fig. 1d). In addition, the second formation peak was observed just above 0.6 V for DME-based electrolytes (marked by arrow "b" in Fig. 1d). Both reduction peaks > 0.6 V for the DME electrolytes in the 1st CV cycle are irreversible, as seen in Figs. 1e and 1f. To unravel the formation mechanism for these two reduction peaks above 0.6 V for the glyme electrolytes necessitates further studies. It is also worth noting from Figs. 1e and 1f that the reduction current densities of the DME electrolytes are slightly smaller than the Gen2 electrolyte in the subsequent CV cycles. This could indicate a denser or better coverage of the SEI formed on the a-Si surface in DME-based electrolytes.
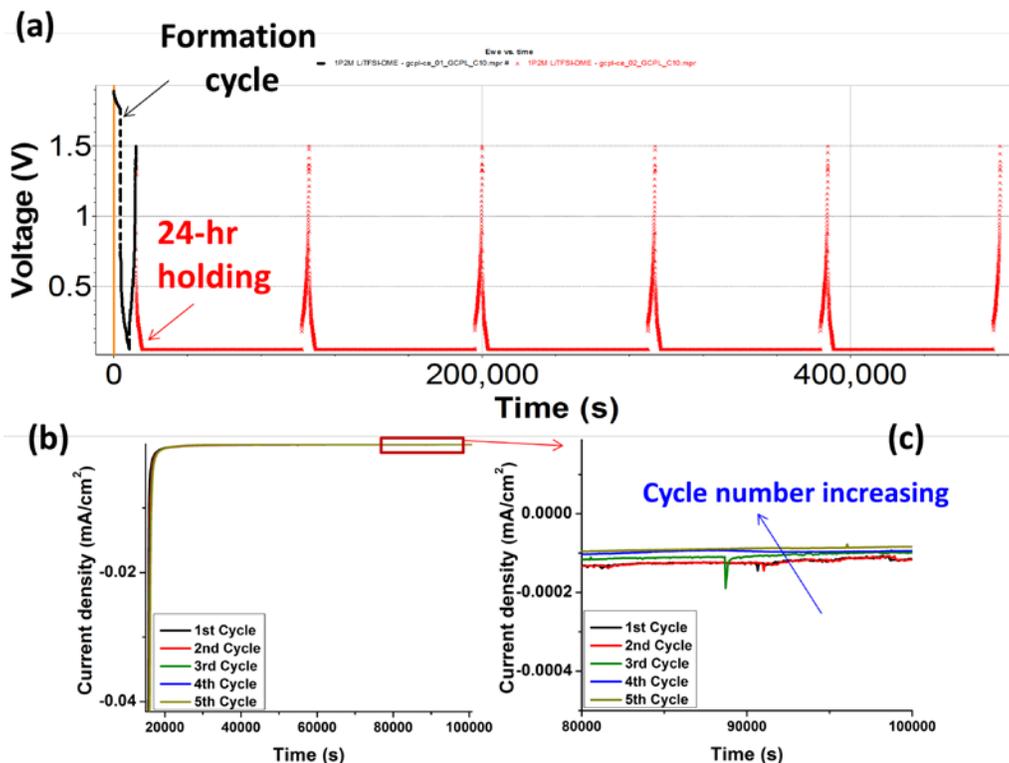
Figure 2. (a) The overview of the voltage-time profile of the galvanostatic cycling (GC)—chronoamperometry (CA) test for a-Si in LiTFSI-DME electrolyte. During the formation cycle, the a-Si was discharged to 50 mV from OCV. Then the a-Si anode was cycled between 1.5 V and 50 mV galvanostatically. In between each charge-discharge cycle, a 24-hour voltage holding (at 50 mV) CA stage was inserted and the current change during this stage was monitored. The galvanostatic current was set at 1C-rate (41.7 μA/cm^2). (b) The current profile from each CA stage (time overlapped). (c) A magnified view of the CA current profile at the end of the voltage-holding stage.

To further evaluate the SEI passivation efficiency on the a-Si anode using different electrolytes, a galvanostatic cycling (GC)–chronoamperometry (CA) test was performed. A typical voltage-time profile of the GC-CA test is shown in Fig. 2a. The current change during the CA stage was shown in Fig. 2b. Immediately after the cell was held at 50 mA, the current decreased rapidly in the first one hour. At the end of the CA stage, the current almost reached an equilibrium value, evidenced by the long plateau in Fig. 2b. The equilibrium current at the stage is assumed to stem from the parasitic reaction of the electrolyte with the lithiated a-Si anode, with the absolute value of the current density quantifying the rate of the parasitic reaction rate. Figure 2c shows that the equilibrium current density decreases upon more cycles, indicating a better SEI coverage on the surface of the a-Si. The same trend was observed for the Gen2 electrolyte. This suggests that the SEI layer grows more "robust" in the first five cycles for the Gen2 electrolyte and LiTFSI-DME. However, the parasitic current density

sharply decreased for the first three cycles for $LiPF_6$-DME electrolyte, and then increased for the last two cycles (see Fig. 3). We ascribe this phenomenon to the SEI dissolution into the electrolyte after the third cycle for $LiPF_6$-DME electrolyte. Clearly, the SEI formed on a-Si in $LiPF_6$-DME electrolyte is not stabilized for the first five GC cycles.

Our future plan of the research includes studying the surface chemistry of the a-Si after the GC-CA test using infrared and X-ray photoelectron spectroscopy to unravel the SEI formation mechanism in different electrolytes proposed here. Nuclear magnetic resonance will be used to elucidate the SEI dissolution in $LiPF_6$-DME electrolyte. In addition, a long-term galvanostatic cycling study is ongoing to evaluate the a-Si thin-film passivation and corrosion behavior in different glyme-based electrolytes. The results will be reported in due course.
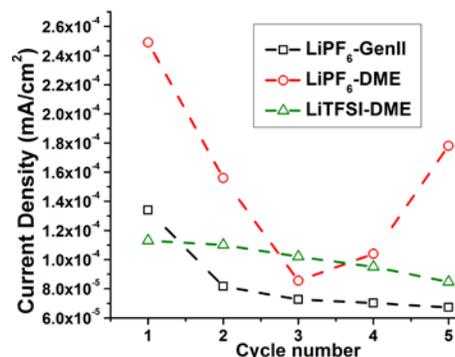
Figure 3. Summary of the parasitic current density with respect to the cycle number for the GC-CA test for various electrolytes.

Conclusions

In summary, a-Si thin film was used as a model anode to investigate its passivation and corrosion behavior in glyme-based electrolytes. CV profiling indicates that the DME-based electrolytes passivate a-Si during early-stage electrochemical cycles. However, the initial GC-CA test clearly indicates that the SEI formed on a-Si in $LiPF_6$-DME electrolyte is unstable compared to Gen2 and LTFSI-DME electrolytes.

References

[1] Miao, J.; Thompson, C. V., Kinetic study of the initial lithiation of amorphous silicon thin film anodes. *J. Electrochem. Soc.* **2018,** *165* (3), A650–A656.

[2] Nie, M.; Demeaux, J.; Young, B. T.; Heskett, D. R.; Chen, Y.; Bose, A.; Woicik, J. C.; Lucht, B. L., Effect of vinylene carbonate and fluoroethylene carbonate on SEI formation on graphitic anodes in Li-ion batteries. *J. Electrochem. Soc.* **2015,** *162* (13), A7008–A7014.

Silicon Electrolyte Interface Stabilization (NREL) - FY19, Q2

Yanli Yin, Caleb Stetson, Andrew Norman, Chun-Sheng Jiang, Mowafak Al-Jassim, and Anthony Burrell (NREL)

Background

In real applications such as the power supply of electrical vehicles, lithium-ion battery cells will frequently experience long rests at various temperatures ranging from -40°C to 60°C. The temperature dependence on the solubility of solid-electrolyte interphases (SEIs) in electrolyte is vital to the understanding of the lithium-ion battery because SEI is critical to battery reversibility. The investigation of SEI behavior on silicon (Si) is of particular interest due to the high theoretical energy storage densities when compared to current graphite electrodes. To understand SEI evolution at varied temperatures on Si electrodes, two problems must be answered. First, SEI formation generally occurs during the silicon lithiation process. The large volume change leads to the mechanical cracks and morphological changes of Si anodes, which creates "new" surfaces being exposed to the electrolyte. The electrochemically induced surface-area changes make it difficult to distinguish the real chemical and electrochemical behavior of SEI without the interference of ever-evolving surface morphology. To investigate the SEI formation before lithiation of Si, a special cutoff voltage may be introduced to the electrochemical protocol. The SEI is well known to form from the electrolyte reduction starting at around 0.9 V. However, the lithiation of silicon (Si) electrode initiates from lower than 0.1 V in the first crystal-amorphous phase transformation.

In our previous work, the SEI formation behavior was verified, able to be decoupled from the Si lithiation behavior by using a high cutoff voltage (0.115 V) protocol. This SEI, defined as the early-stage SEI, was established as a layer of species showing the chemical composition and electrochemical behavior that is similar to the SEI formed on the lithiated electrode. Therefore, the early-stage SEI is a perfect model for the independent research of the evolution of SEI at varied temperatures. Second, it is important to know more about the electronic properties of SEI at various temperatures because an electronically insulating and ionically conductive SEI is capable of passivating the electrode against further reactions with the electrolyte. Many techniques have been used to monitor the insulating performance changes of SEI at varied temperatures. As reported by Zhang et al., the lithium-ion battery working at low temperature (-30°C) was studied by using electrochemical impedance spectroscopy, which shows the significant temperature dependence of charge-transfer resistance.[1] As Dahn et al. reported, more inorganic species were observed in the SEI of the negative electrodes that spent longer at 60°C, suggesting that $LiPF_6$ reacts with carbonates in the SEI to create a more inorganic SEI over time.[2] These methods can only establish the changes to resistance for the entire cell. Thus, the evaluation of insulating behavior of SEI was combined with electrolyte and electrode in the cell results. To probe the insulating behavior of the SEI itself, scanning spreading resistance microscopy (SSRM) 3-D resistivity vs. depth profiling was presented as a methodology to investigate the electronic properties and thickness of SEI.[3]

In this work, we used a special protocol to decouple the lithiation-induced Si deformation from the SEI formation through setting a high cutoff voltage of 115 mV for the galvanostatic reduction process of the Si electrode. After the process of this early-stage SEI formation, the Si electrode was rested for a long time at varied temperatures. The solubility of SEI at varied temperatures was addressed without involving Si electrode deformation, which is a novel approach that has not been reported. The SSRM 3-D resistivity vs. depth profiling is used to study this temperature-dependent solubility of SEI by monitoring its electrical conductivity distribution and thickness evolution. We also investigated the morphology of the Si surface using atomic force microscopy (AFM) to address the heterogeneous distribution and evolution of SEI dissolution during long resting times at different temperatures.

Results

Experimental Method. Silicon model samples with a native SiO_x layer established in FY17 have been used in this study. All of the silicon electrodes (½ inch x ½ inch) were cleaned with our established multi-step cleaning

protocol to remove the surface grease, particles, and organic residue. After cleaning, the electrodes were dried in a vacuum oven at 100°C prior to the cell fabrication. The electrolytes selected for this research are 1.2 mol/L $LiPF_6$ (abbreviation "G2" used in the plots) dissolved in the solution comprising ethylene carbonate (EC): ethyl methyl carbonate (EMC) with the weight ratio of 3:7, respectively. All of the Si electrodes were used as working electrodes in the customized electrochemical cells, where the lithium metal was used as a counter electrode. 7 μL of the electrolyte were used in every cell, and the Celgard 2325 was used as a separator for the cell assembly. After cycling, samples were dismounted, washed in dimethyl carbonate (DMC) for two minutes, dried in vacuum for one hour, then transferred to a glovebox AFM through a system of gloveboxes and vacuum chambers to avoid exposure to atmosphere.

Results and Discussion

The electrochemical behavior of early-stage SEI formation. Here, we use the single-crystalline Si wafer electrodes with a native SiOx layer as a work electrode and assembled the half cells with the lithium metal as counter in this study. We elaborated on the preparation and cleaning protocol for the Si in the Experimental section. The constant current charge and discharge processes were run at a current density of 6.82 μA cm^{-2} as the following protocol: i) Give reduction current of 6.82 μA cm^{-2} to the cutoff voltage at 115 mV, followed by a 3-hour rest. ii) Repeat 1) for 50 cycles. iii) Give current 6.82 μA cm^{-2} to 115 mV, hold at 115 mV for 10 minutes. Cells were run at 25°C from step i) to iii). iv) Varied resting for 45 hours at temperatures of 25°C, -10°C, and 50°C, respectively. A sample without resting was used a control. After being disassembled, samples were gently washed in DMC for 2 minutes, dried in the vacuum chamber for 1 hour, and immediately transferred into the SSRM system via an air-free transfer mechanism.
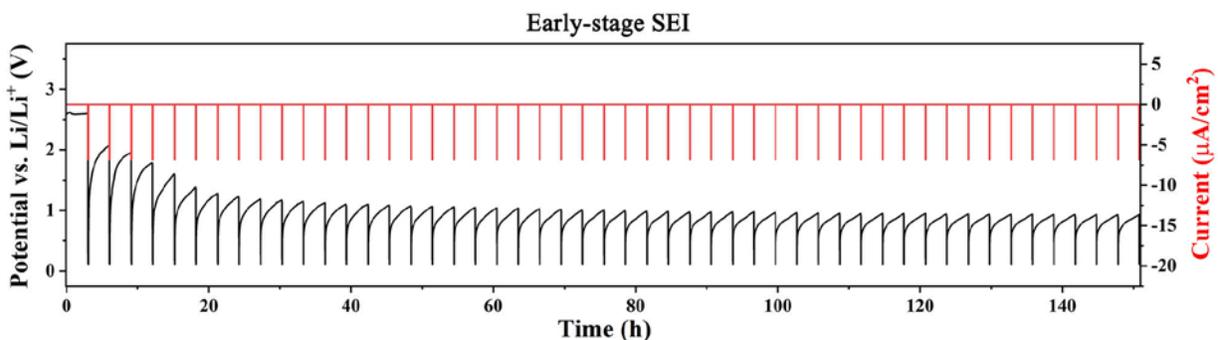
Figure 1. The voltage and current profiles of the Si electrode in 50 cycles of early-stage SEI formation. In every cycle, the cell voltage quickly touches 115 mV followed by a slow returning back during the 3-hour rest. The final cell voltage at the end of 3-hour rest was remarkably reducing in the first 10 cycles. At the 10th cycle, the cell voltage returns back to the final value of around 1.0 V during 3-hour rest. After the 10th cycle, the final returning back cell voltage is stable, indicating that the formation and dissolution of SEI is in balance. This verifies a constant cell status for initiating the resting measurement at various temperatures.
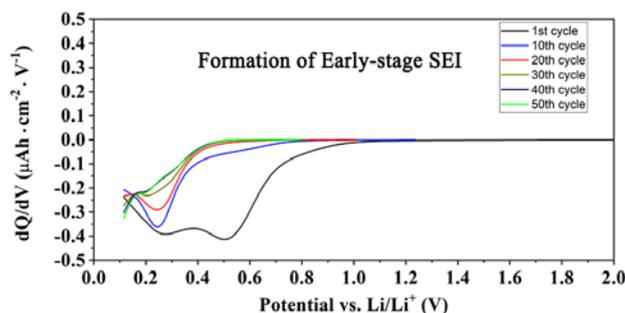
Figure 2. The differential capacity profile of the voltage profile of silicon electrode in 50 cycles of early-stage SEI formation.

Figure 2 shows the differential capacity profile of silicon electrode in 50 cycles of early-stage SEI formation. In the first cycle, reduction peaks were observed at around 550 mV and 250 mV. The reduction peak at 550

33

mV is associated with the reaction of electrolyte reduction. The reduction peak at 250 mV might be associated with the reaction of native SiO_x. During the subsequent cycling, the peak at 550 mV disappears after about 20 cycles, whereas the peak at 250 mV reduces slowly and disappears after the 50th cycle. This further verifies the balanced cell status for initiating the resting measurement at various temperatures.
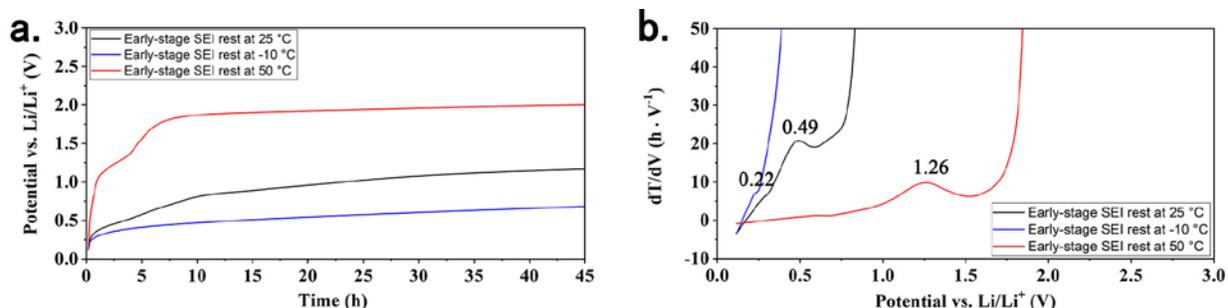
Figure 3. (a) The voltage profile and (b) the differential time of silicon electrode during the 45-hour resting at the temperature of 25°C, -10°C, and 50°C after 50 cycles of early-stage SEI formation.

Figure 3a shows the voltage profiles during the 45-hour resting at the temperature of 25°C, -10°C, and 50°C after 50 cycles of early-stage SEI formation. During the first few minutes resting, the voltage of the cell rested at 50°C returns back to higher than 1.0 V, whereas the voltage of the other two cells is lower than 0.5 V. After the first 10 hours of resting, all cell voltages reach a low slope of increasing voltage. Dissolution shows a higher rate during the first few minutes compared with the rest of process. After the 45-hour rest, all cell voltages return back to a higher value compared with the initial 0.115 V. The final cell voltage is higher at the higher temperature, indicating that the SEI components were dissolved or detached with faster kinetics at the higher temperature.

Figure 3b shows the differential capacity profiles during the 45-hour rest at the temperatures of 25°C, -10°C, and 50°C after 50 cycles of early-stage SEI formation. The profile of cells at of 25°C, -10°C, and 50°C shows peaks at 0.49 V, 0.22 V, and 1.26 V, respectively. The peaks are attributed to the stabilized voltage of SEI component reactivity at varied temperatures. The cell at higher temperature shows a higher characteristic peak, indicating that the dissolved or detached SEI components have different chemistry at different temperatures.

***Ex-situ* AFM-SSRM characterization of SEI.** We carried out AFM and SSRM measurement on the Si electrode with 50 cycles of early-stage SEI formation followed by no resting and resting for 45 hours at various temperatures of -10°C, 25°C, and 50°C.
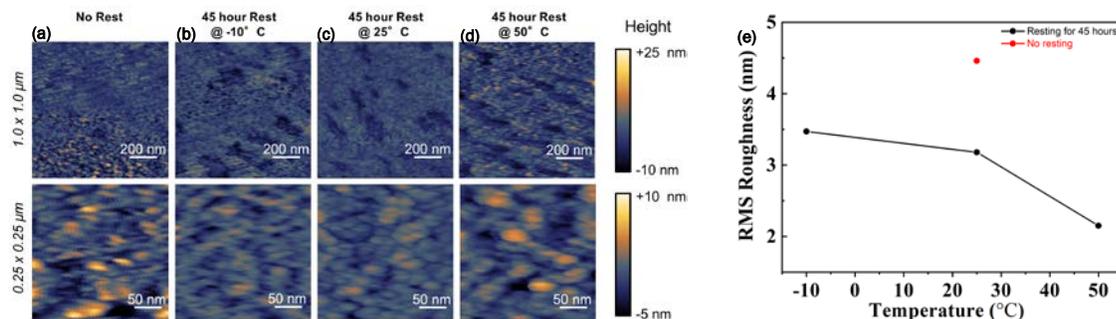
Figure 4. The AFM surface morphology of Si electrode with 50 cycles of early-stage SEI formation followed by (a) no resting, and resting for 45 hours at varied temperatures of (b) -10°C, (c) 25°C, and (d) 50°C, and (e) the RMS roughness.

Figures 4a–d show the AFM surface morphology. The unrested sample shows more heterogeneous morphology compared with the resting samples. By comparing all the rested samples, the sample at higher temperature shows less heterogeneous morphology. This was verified by the RMS roughnesses shown in Figure 4e, which were calculated from 5x5 μm AFM images. The unrested sample shows higher RMS

roughness compared with the rested samples. By comparing all the rested samples, the sample at higher temperature shows lower RMS roughness. This indicates a faster dissolution of SEI at higher temperatures during the resting and possible "smoothing" of the original unrested surface.
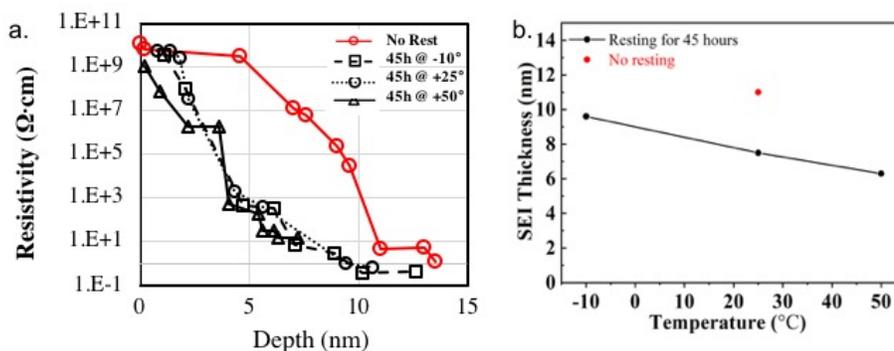
Figure 5. (a) SSRM 3-D resistivity vs. depth profiles and (b) the SEI thickness of Si electrode with 50 cycles of early-stage SEI formation followed by no resting, and resting for 45 hours at varied temperatures of -10°C, 25°C, and 50°C.

Figure 5a shows the resistivity profile as the function of depth profile. From this profile, we obtained the SEI thickness data shown in Figure 5b. The unrested sample shows higher SEI thickness compared with the rested samples. The rested samples show lower thickness at higher temperatures, indicating greater dissolution of the SEI into the electrolyte.
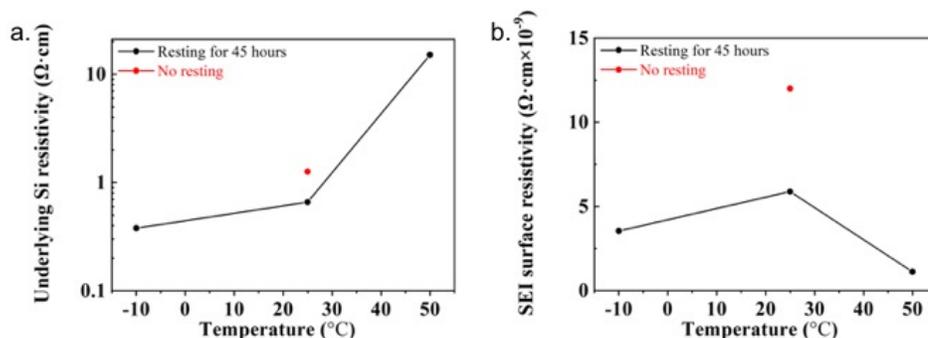
Figure 6. The resistivity of (a) underlying Si and (b) SEI surface of Si electrode with 50 cycles of early-stage SEI formation followed by no resting, and resting for 45 hours at various temperatures of -10°C, 25°C, and 50°C.

Figure 6 shows the resistivity of (a) underlying Si (beneath the SEI) and the (b) SEI surface of Si electrode. The unrested sample shows similar resistivity of underlying Si compared with the rested sample at 25°C. As shown in Figure 6a, the rested sample shows a higher resistivity of the underlying Si at higher temperatures. This may be attributed to the faster rates of diffusion allowing for "fouling" of Si with species such as fluorine, resulting in a loss of electronic conductivity. A control experiment on the Si electrodes without cycling is planned to verify this hypothesis. As shown in Figure 6b, the unrested sample shows a more resistive SEI surface compared with all the rested samples.

Conclusions

In summary, we formed the early-stage SEI on the Si electrode by using the high cutoff voltage protocol, never allowing the potential vs. Li/Li^+ to drop below 115 mV. The electrochemical behavior of the Si electrode was monitored during the long rest, followed by the early-stage SEI formation. Based on the electrochemical profile during the long rest, the SEI may be dissolved or detached with higher SEI dissolution rates at higher temperatures. Analysis of AFM and SSRM data shows that resting of the early-stage SEI results in a less heterogeneous morphology, lower roughnesses, and reduced final thicknesses at higher resting temperatures.

This confirms faster dissolution rates of SEI at higher temperatures. The rested samples also demonstrate minor shifts in SEI surface resistivity of the underlying Si at higher resting temperature that need to be further investigated through control experiments.

References

[1] Zhang, S. S.; Xu, K.; Jow, T. R., Electrochemical impedance study on the low temperature of Li-ion batteries. *Electrochimica Acta* **2004,** 49, 7, 1057–1061.

[2] Ellis, L. D.; Allen, J. P.; Hill, I. G.; Dahn, J. R., High-Precision Coulometry Studies of the Impact of Temperature and Time on SEI Formation in Li-Ion Cells. *Journal of The Electrochemical Society* **2018,** 165, 7, A1529–A1536.

[3] Stetson, C.; Yoon, T.; Coyle, J.; Nemeth, W.; Young, M.; Norman, A.; Pylypenko, S.; Ban, C.; Jiang, C.; Al-Jassim, M.; Burrell, A., Three-dimensional electronic resistivity mapping of solid electrolyte interphase on Si anode materials. *Nano Energy* **2019,** 55, 477–485.

Part 3. The Soluble Species

Reactivity and Evolution of the Silicon-Electrolyte Interphase (SiEI) and Nature of the Soluble SiEI Components during Cycling (NREL and SNL)

Sang-Don Han, Bertrand Tremolet de Villers, Kae Fink, Shriram Santhanagopalan (NREL), and Christopher A. Apblett (SNL)

Background

Due to complexity, high reactivity, and continuous evolution of a silicon-electrolyte interphase (SiEI), it remains a poorly understood topic in advanced Li-ion battery research; its detailed and real-time analysis is a great challenge. Vibrational spectroscopy is one of the most important avenues for understanding and quantifying the interfacial chemical and electrochemical reactions. Raman and infrared (IR) spectroscopy are attractive due to their versatility, and they are used extensively by the battery community in their *ex-situ* form. Developing *in-situ* methods of these techniques, however, will provide new insight and help in elucidating the mechanism of interfacial failure in battery systems. Moreover, combining *in-situ* analysis from both Raman and IR spectroscopy will provide detailed and complementary information. Raman spectroscopy relies on polarizing the electron cloud associated with a chemical bond, rather than measuring the associated dipole moment (as in IR spectroscopy). Therefore, the combination of these two techniques in one study enables analysis that may otherwise be missed by applying only a single technique.

Another analytic technique to study degradation mechanisms in Li-ion batteries is gas chromatography-mass spectrometry (GC-MS). This has been used by others in the past to study electrolyte degradation and elucidate probable decomposition mechanisms.[1] Here, we attempt to use GC-MS to identify SiEI components that dissolve in the electrolyte during cycling. Using a custom-built three-electrode testing cell, we sample the electrolyte solution at various stages of battery cycling, then analyze the solution for degradation products. These studies can provide guidance in stabilizing the SiEI by understanding the underlying chemistry and physics and providing a mechanical explanation of surface chemistry and various reactions/interactions within the SiEI.

Results

I. Reactivity and Evolution of the Silicon-Electrolyte Interphase (SiEI) - *in-situ* Raman Microscopy
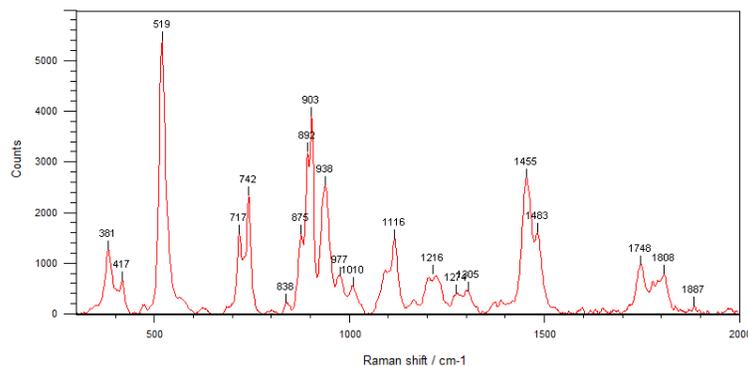
Figure 1. Representative Raman spectrum with an *in-situ* cell. Observed peaks were assigned to the sapphire window (381 and 417 cm^{-1}), a strong signal from the crystalline silicon wafer anode (519 cm^{-1}), and many peaks assigned to the various components of a standard Gen2 electrolyte (1.2M LiPF$_6$ in 3:7 ethylene carbonate (EC): ethyl methyl carbonate (EMC) wt%).

Table 1. Raman peak assignments

Raman Band Center (cm^{-1})	Assignment	Species of Origin	Reference(s)
380	E_g	Al_2O_3 (from sapphire window)	1
417	A_{1g}	Al_2O_3	1
431	E_g	Al_2O_3	1
450	E_g	Al_2O_3	1
472		PF_6^-	4, 5
480, very broad		a-Si (amorphous silicon)	
513		?	
520	1TO	c-Si (crystalline silicon)	
530		?	
556		PF_6^-	4
570		PF_6^-	4
578	E_g	Al_2O_3	1
645	A_{1g}	Al_2O_3	1
720	o, O-C-O	EC (ethylene carbonate)	2
728	o, O-C-O	FEC (fluoroethylene carbonate)	2
733	o, O-C-O	EC···Li$^+$	2, 6
740	υ, P-F	PF_6^-	2
742	υ, P-F	PF_6^-···Li$^+$	2,4
748	E_g	Al_2O_3	1
868	υ, C-F	FEC	2
897	β, C-C	EC	2
903		EMC (ethyl methyl carbonate)	this work, 3, 5
905		EMC···Li$^+$	6
908	β, C-C	FEC	2
932	δ, O-C-O	EMC	3, this work
945	δ, O-C-O	EMC···Li$^+$	3, this work
970		EC	6
1455		?	
1488	δ, CH$_3$	EC	2
1705–1730	υ, C=O	EMC···Li$^+$	3, this work
1748	υ, C=O	EMC	3, this work
1778	υ, C=O	EC	2
1804	υ, C=O	EC	2

Notation: υ = stretching, δ = bending, o = ring breathing; β = ring deformation

References: (1) DOI:10.1063/1.367972, (2) DOI:10.1021/acsnano.8b05038, (3) DOI:10.1039/C6CP07215A, (4) DOI: 10.1021/acs.jpcc.5b00826, (5) DOI: 10.1023/A:1005151220893, (6) DOI: 10.1016/j.jpowsour.2014.05.107

Initial Measurements and Peak Assignments. Figure 1 shows a typical Raman spectrum collected through an *in-situ* Raman cell. We have invested time to build a reference table for peak assignments (Table 1) and continue to refine it (updated from last report).

Electrochemical Cycling Tests with an in-situ Cell. For *in-situ* Raman measurement, a crystalline silicon wafer (c-Si, 525 µm, <0.005 Ω cm, p-type) strip and a lithium metal foil were used as the working and the counter/reference electrodes, respectively. Raman spectra were collected at various voltages and times during galvanostatic cycling (at 5 µA) of the *in-situ* cell. The open-circuit voltage (OCV) of the assembled cell was at around 2.85 V *vs.* Li/Li$^+$ (hereafter), which is usually observed from coin-type or other-type cell cycling tests (Fig. 2). Upon the 1st discharge (2.85–0.11 V), electrolyte decomposition and initial SiEI formation were observed at between ~1.3 and 0.11 V. Then, lithiation of c-Si (c-Si + xLi → a-Li$_x$Si) was observed at around 0.115 V for 4.5 h, as programmed. Upon the 1st charge (0.11–1.50 V), low-voltage and high-voltage delithiation plateaus of amorphous Si were observed, as shown in a previous study:[2] a-Li$_{(x'+x'')}$Si → a-Li$_{x'}$Si + x''Li and a-Li$_{x'}$Si → a-Si + x'Li. In the case of Raman spectra during discharging and charging, we observed a reduction of the c-Si peak at 520 cm^{-1} and an increase in a broad feature that may be a-Si (broad, centered ~480 cm^{-1}). Note that we now have repeated this procedure at least three different times, and with this configuration, we observed similar electrochemical behavior of our samples in each instance.
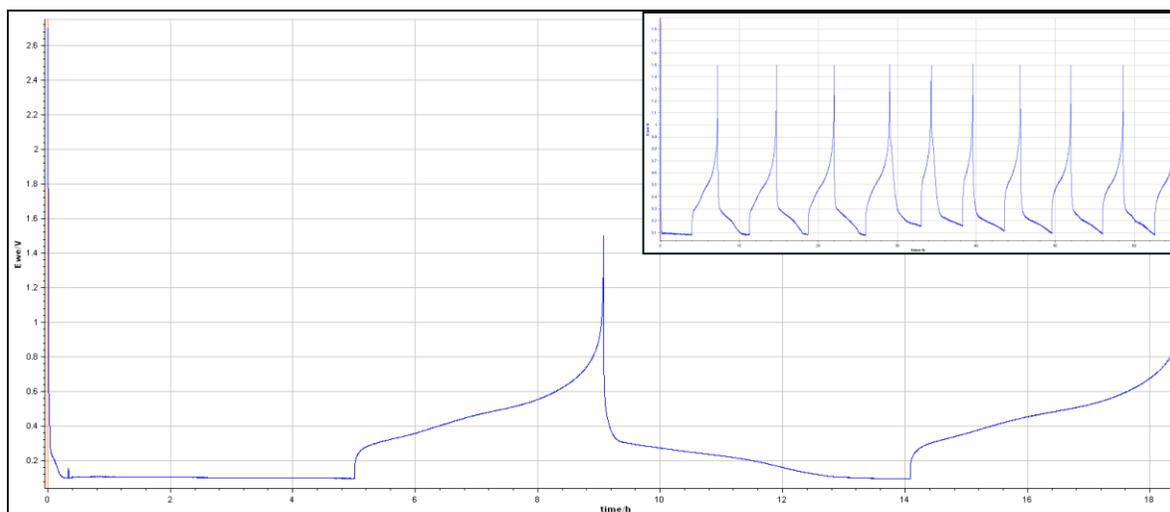
Figure 2. Typical galvanostatic cycling of the *in-situ* Raman cell. Inset shows the first 10 cycles.

Problems Encountered and Mitigating Strategies. We are still exploring optimal measurement parameters, such as sample position, light-excitation intensity, collection time, spectra averaging, and objective height, because of excitation-beam damage and weak signal-to-noise (S/N) ratios for some important electrolyte component scattering bands (e.g., EMC coordinated with Li$^+$ in the region of 1700–1740 cm^{-1}). To increase our signals, we are trying different combinations of light-excitation intensity (1–50 mW), collection time (2–300 s), and spectra averaging (3–50 accumulations). Increasing the excitation intensity certainly increases the S/N ratio, but can easily damage the samples. Figure 3 shows three possible sample measurement positions: over the electrolyte region (left), at the edge of the silicon (middle), and on top of the silicon but still near the interface with the electrolyte (right). Measuring on the electrolyte, we observe a Raman spectrum representative of electrolyte. The problem with this position is that we are unable to determine if we are probing the Si/electrolyte interface region or only bulk electrolyte where changes are unlikely. Alternatively, we have tried measuring right at the edge of the silicon wafer. Initially, this yields a good Raman spectrum that includes electrolyte peaks and the 520 cm^{-1} c-Si peaks, with similar intensities. However, as we continue to measure in this position, the sample is often damaged by the laser excitation, even at the lowest practical laser powers (e.g., ~1 mW at 532 nm). We have found the best compromise to be the third option for position,

which is on top of the silicon wafer. The top of the wafer is wet by a thin layer of electrolyte and we are certain that our excitation spot is at the Si/electrolyte interface. In addition, the wafer here seems more robust to beam damage, although not completely (Fig. 4a). To minimize beam damage, we move to a new spot on the wafer surface for each measurement. Doing this, we see very little evidence of beam damage, as shown in Fig. 4c. The major drawbacks of choosing this sample position are that the c-Si scattering peaks are very strong such that the peak shoulders mask nearby electrolyte peaks (Fig. 3, right figure), and also, that inhomogeneity of the silicon surface can yield spot-to-spot variation in the Raman spectra, as shown in Fig. 4b. Nevertheless, we believe this is the best compromise.
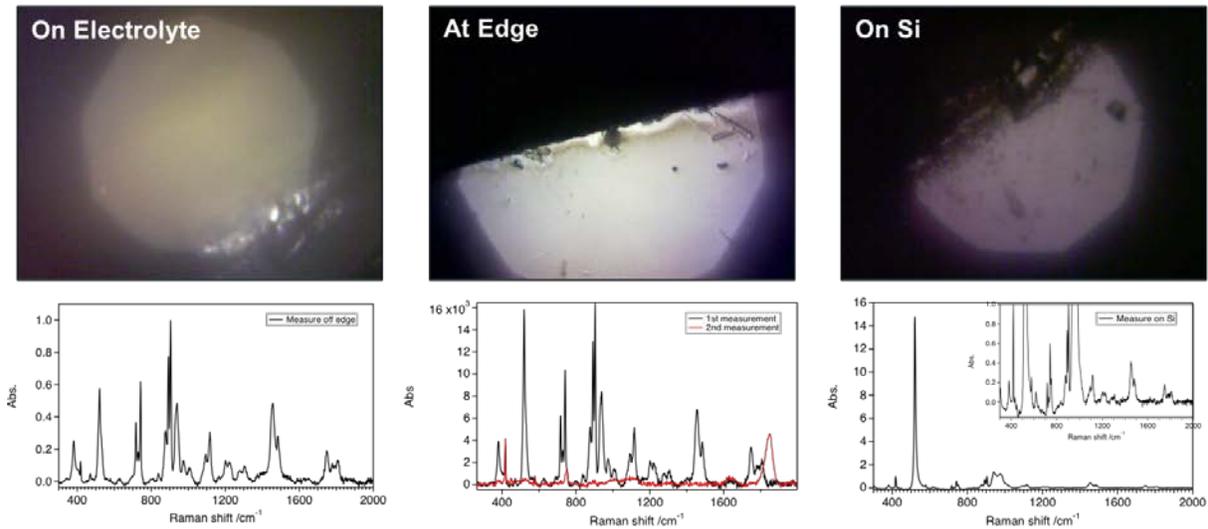
Figure 3. Optical micrographs of the various sample positions for Raman scattering measurements and the corresponding spectra collected at those positions.
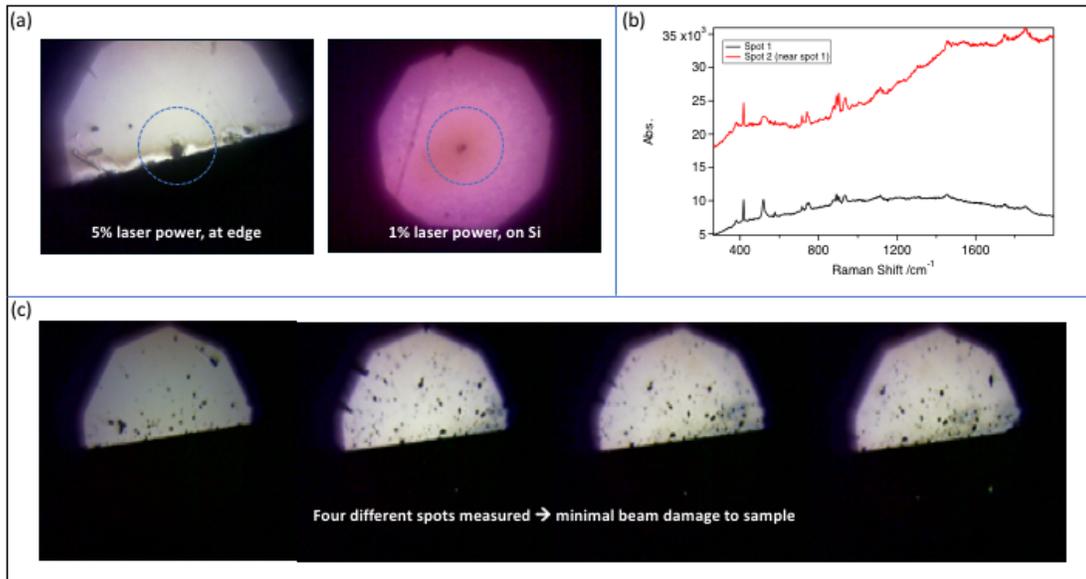
Figure 4. (a) Evidence of excitation-beam-induced damage for two different sample positions and laser excitation powers. (b) Two adjacent spots on the silicon wafer surface can yield different Raman spectra due to surface inhomogeneity. (c) Moving to a new spot for each measurement minimizes beam damage to the sample.

Data Processing. Once we collected satisfactory Raman scattering data, we needed to process them. One challenge is background subtraction because broad backgrounds appear in some spectra, probably due to fluorescence of decomposition products in the electrolyte. The approach we have developed is to manually fit a spectrum with a custom, high-order polynomial, then apply the node of that function to all spectra within the dataset. This approached is demonstrated in Fig. 5.
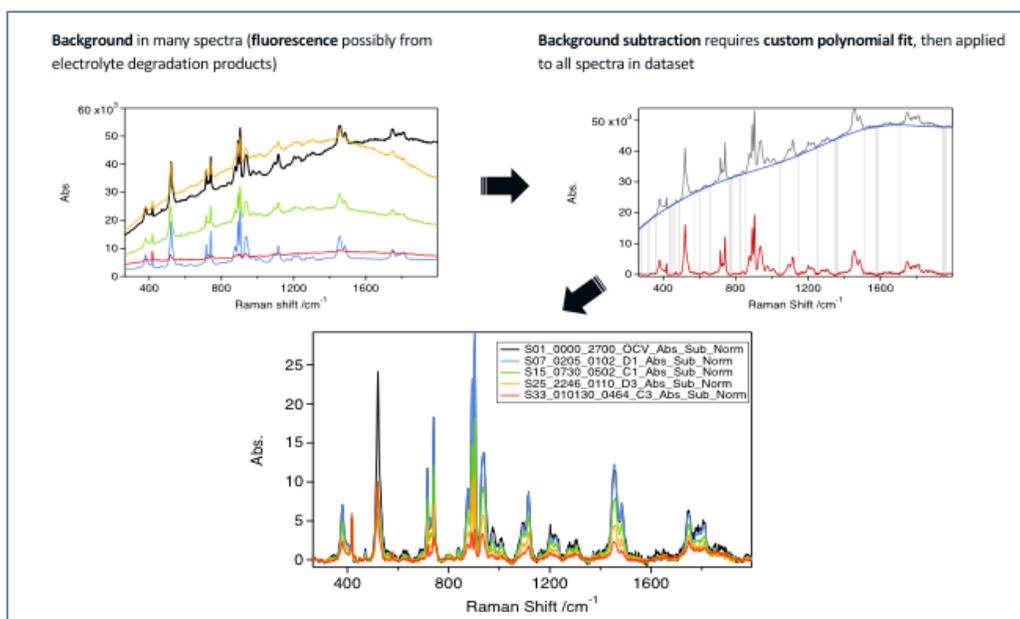
Figure 5. Method we employ to background subtract our Raman data.

After background subtraction, we must then choose where to normalize the spectra. Figure 6 shows a comparison of normalizing to the strongest electrolyte peak, EC at 905 cm^{-1} vs a peak from the sapphire window at 419 cm^{-1}. We decided to use the latter because the sapphire should be relatively invariant in our measurements.
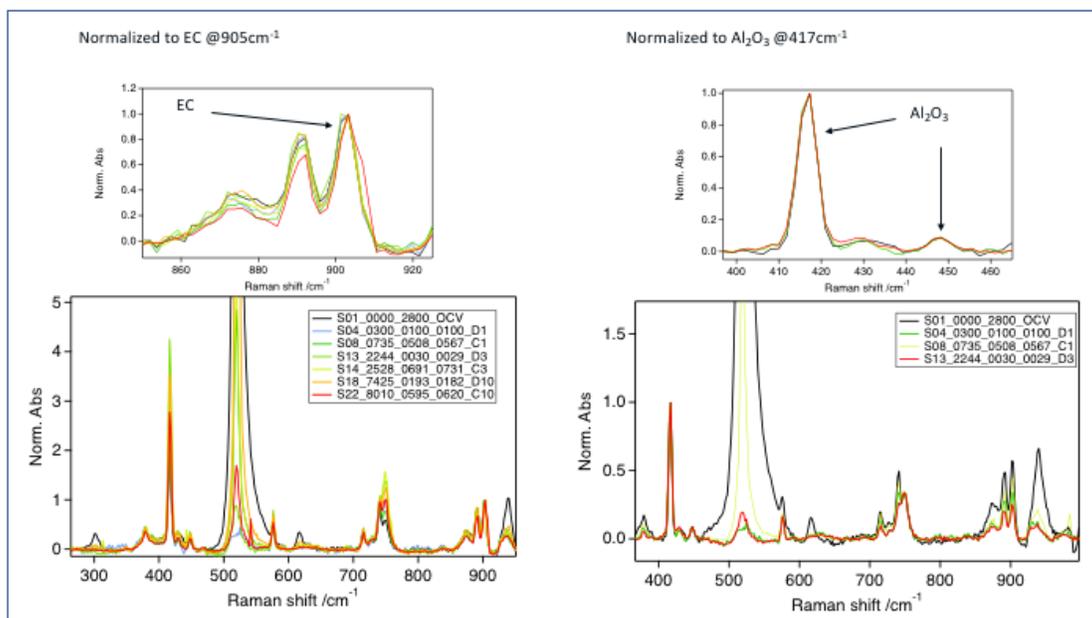
Figure 6. Comparison of normalizing the Raman spectra at the EC peak of 905 cm^{-1} *vs.* the sapphire window peak of 419 cm^{-1}.

41

Raman Spectra during Cell Cycling. Figure 7a shows a series of Raman spectra collected during the battery cycling. Overall, we have observed three things in our repeated Raman measurements. Generally, most of the peaks decrease over time, regardless of whether we are charging or discharging the battery. Our concern is that our cell might not be completely sealed and that we are slowly losing electrolyte to evaporation. Alternately, we could be degrading the electrolyte due to incident-beam heat dissipation and damage. However, we do not observe any new peaks appearing over time that could be from electrolyte decomposition, or from newly formed SiEI species. Despite losing signal over time, we do observe some quasi-reversible behavior of the EC/EMC solvents and the PF_6^- anion. As seen in Fig. 7b, solvent-separated ion pairs (SSIPs) of free PF_6^- anions (Li^+ cation and solvent molecules) (at 740 cm^{-1}) decrease during discharging, but increase somewhat reversibly during charging. Conversely, the adjacent peak around 742 cm^{-1} attributed to PF_6^- anion and Li^+ cation aggregates (AGGs) increases during discharging and decreases during charging (Table 1).
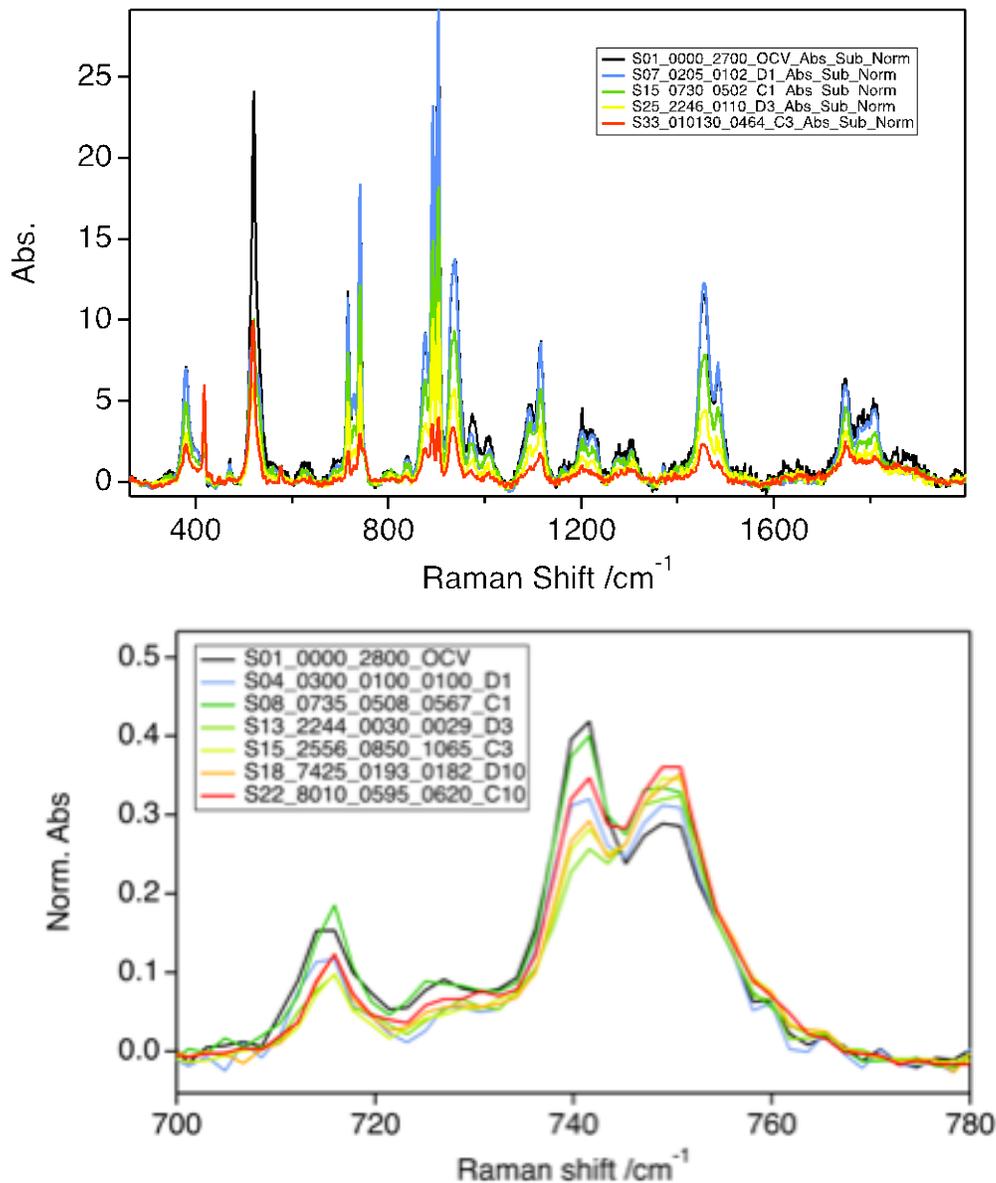
Figure 7. (a) Typical series of *in-situ* Raman spectra after background subtraction and (b) quasi-reversible coordination behaviors of the PF_6^- and Li^+ cation at 740 cm^{-1} (SSIP) and 742 cm^{-1} (AGG), respectively.

II. Nature of the Soluble SiEI Components during Cycling - Gas Chromatography-Mass Spectrometry

Cell and Instrumentation Details. For our GC-MS study, we are using a custom three-electrode Swagelok-type cell, nicknamed the "x-wing cell." This cell was designed and built by Dr. Christopher Apblett at Sandia National Laboratories. Shown in Fig. 8, the cell consists of three PEEK-covered stainless-steel electrode rods with Swagelok compression fittings. In addition, there are two Luer fittings that allow us to sample the electrolyte in the cell while it is actively cycling. Finally, each side has an optical window for *in-situ* spectroscopy such as Raman microscopy (potential future work).

For our initial measurement, we used a 7×7 mm piece of monocrystalline silicon wafer (boron-doped, 0.005 Ω cm) as the working electrode. The counter and reference electrodes were Li metal foil. Whatman glass microfiber was used for the separators. The Gen2 electrolyte consisted of 1.2M $LiPF_6$ salt dissolved in a mixture of EC:EMC (3:7 wt%). Note that the current design of the x-wing cell requires about 4 mL of

Figure 8. Custom three-electrode Swagelok-type cell.

electrolyte to fill up the entire cell space. We used ~2 mL and periodically agitated the cell to distribute the electrolyte around the electrodes and ensure that the separators stayed saturated with electrolyte. Electrochemical testing and the addition/removal of electrolyte to/from the x-wing cell was done in an argon-filled glovebox. Electrolyte solution samples were placed in 4 mL glass vials, and then caps with PTFE septa were crimped onto the vials to seal them before removing them from the glovebox (Fig. 9a). Sample analysis was done with an Agilent 7890B gas chromatograph and Agilent 5977B single-quadrupole mass selective detector. The temperature profile for the GC was taken from Reference 1. Molecular species were determined by searching the mass spectra within a NIST database (MassHunter software).

Figure 9. (a) GC-MS samples: 1) fresh Gen2 electrolyte, 2) electrolyte soaked in x-wing cell for 36 hours at OCV, 3) electrolyte removed at the end of the 1st discharge half-cycle (~4 hours/0.05 V), and 4) electrolyte removed near the end of the first charge half-cycle (~4 hours 25 mins/0.8-1.2 V). (b) Gas chromatogram for the four electrolyte solution samples (inset: zoom-in at long retention times). (c) Galvanostatic cycling data (applied current = 50 µA cm-2).

Initial Electrochemical Cycling and GC-MS Results. In our initial study, we compared four different electrolyte solution samples with GC-MS (Fig. 9a): Sample #1 was a control sample of just Gen2 electrolyte; Sample #2 was electrolyte that was soaked in the x-wing cell at open-circuit conditions for 36 hours; Sample #3 was taken during galvanostatic cycling, at the end of the 1st discharge half-cycle (~4 h/0.05 V); and Sample #4 was taken near the end of the 1st charge half-cycle (~4 h 25 min/0.8–1.2 V). Visually, it appears that Samples #2 and #3 are somewhat cloudy compared to just Gen2 electrolyte, suggesting some additional dissolved species in the solutions. Figure 9c shows the first 8 cycles of galvanostatic testing with the green and blue dots, labeled 3 and 4, respectively, representing when Samples #3 and #4 were taken. With Samples #2–#4, we note that 2 mL of fresh electrolyte were added after each sample. Figure 9b shows the gas chromatograms for each of the four samples. The inset is a zoom-in at the longest retention times. The mass spectra at retention times of 1.67, 4.46, and 15.41 min correspond to the electrolyte components PF_5, EMC, and EC, respectively. Retention times with lower counts represent other electrolyte-related species such as DMC (rinsing solvent between sample injections into the GC) and DEC, a reaction product of EMC and DMC.[1] Additional detected signals are various degradation species of PF_6^-, PF_3O, and $P(CH_2CH_3)O(OH)_2$. From the inset, it is clear that Sample #2 contains species not present in the other samples. Most notably, the peak at 42.6 min is identified as glycerol 1-myristate, a likely degradation product of the linear carbonates. The broad baseline increase starting around 42 min for each sample indicates the presence of water. The last peaks occurring after 46 min are siloxanes, which could come from reactions with the silicon anode, but more likely result from contamination by the silica column in the GC.

Conclusions

Based on extensive literature survey and several initial Raman measurements, we built a reference table for peak assignments of standard Gen2 electrolyte components (e.g., EC, EMC, PF_6^-), additive (FEC), and an *in-situ* cell part (e.g., Al_2O_3), which continues to be refined. Using a well-designed *in-situ* cell, reasonable and meaningful electrochemical performance data were obtained with initial promising Raman data. We will address the issues that we encountered during preliminary *in-situ* Raman measurements by exploring optimal measurement parameters, designing a different shape of Si wafer, and finding an appropriate Raman measurement spot.

The idea of detecting soluble SiEI components with GC-MS remains promising, but we think that improvements in our experimental design are necessary. First, we plan to modify the x-wing cell to require much less electrolyte. Having greater than 2 mL probably dilutes the sample too much, despite the high sensitivity of GC-MS. Additionally, we would like to add a pump to continuously flow electrolyte through the cell. This would have two-fold benefits: 1) it would facilitate sampling by not requiring that we open the Luer fittings to access the electrolyte, and 2) pushing electrolyte through the cell should ensure that we are flowing through the anode/separator region, where SiEI components accumulate. Furthermore, we are exploring possible methods of combustion (e.g., electrospray ionization (ESI-MS)) for higher molar mass species that might be undetectable using just the GC heater. Finally, we planned to investigate how adding small amounts of water to the electrolyte might yield more soluble SiEI components, via HF etching of the anode surface, after HF formation from hydrolysis of $LiPF_6$.

References

[1] G. Gachot et al., *Analytical Chemistry* **2011**, *83*, 478–485.
[2] M. N. Obrovac et al., *J. Electrochem. Soc.* **2007**, *154*, A103–A108.

Chemical and Electrochemical Reactivity of Plasma-Synthesized Silicon Nanoparticles

Mike Carroll, Greg Pach, Fernando Urias-Cordero, Ryan Pekarek, Nathan Neale (NREL)

Background

One of NREL's tasks explores plasma-synthesized silicon nanoparticles (Si NPs) as model systems for Li_xSi anodes. Such plasma-prepared Si NPs are valuable because they feature hydrogen-passivated surfaces and a high surface area resulting from their <10-nm diameter that makes them well suited for chemical reactivity studies using Fourier transform infrared (FTIR) spectroscopy and quantitative off-gassing analysis. These reactivity studies are relevant for understanding early-stage SEI layer growth as well as individual SEI component chemical stability. In early FY19, we continued our prior years' efforts to 1) develop an *operando* attenuated total reflectance (ATR)-FTIR capability for studying early-stage SEI growth and dissolution; 2) increase the size and scale of our Si NP plasma production process; and 3) started a new effort to incorporate plasma-grown Si NPs into batteries.

In Q2 FY19, we stepped back and put new eyes on the *operando* ATR-FTIR tool and have concluded that the key to success can only be found with a highly conductive, infrared-transmitting Si wafer substrate. We continued to push our inductively coupled plasma (ICP) capability with our plasma growth system that has now shown 40.6±6.2 nm diameter Si NPs, albeit at low yield. In addition, we have continued to prepare many batches of smaller ~7-nm-diameter Si NPs to support internal battery-electrode fabrication as well as collaboration with Argonne National Laboratory. Finally, the initial half-cell battery data for air-free electrodes prepared with small-diameter, plasma-grown Si NPs were collected, showing the necessity of mitigating surface reactivity and optimizing the Si:C45 conductive carbon ratio.

Results

Operando *ATR-FTIR Spectroscopy.* In Q2 FY19, we have continued our development of the *operando* ATR-FTIR spectroelectrochemical characterization instrument. Prior work in this area by Ross and coworkers[1,2] showed that the components of the SEI vary significantly as a function of applied voltage. An electrolyte comprising 1.0 M $LiPF_6$ in EC:DEC (1:2, v/v) was used in conjunction with a native oxide (SiO_x)-covered Si wafer. At 1.3 V, electrolyte reduction (DEC) to diethyl 2,5-dioxahexane dicarboxylate (DEDOHC) was found, whereas at 5 mV, selective electrolyte reduction (EC) to lithium ethylene dicarbonate (LiEDC) occurs.[3] Our goal is to extend this study of SEI dissolution and growth using other model samples (H-terminated Si, native SiO_x-terminated, and molecularly functionalized Si wafers) and eventually extend this to three-dimensional Si NP-based electrodes assembled on the Si wafer substrate.

In Q2 FY19, we conducted a further analysis of this 2017 paper. We now believe that the voltages reported in this work are incorrect. In our work developing this capability, we found that an identical 5 Ω•cm Si wafer (same doping density as in the 2017 Lawrence Berkeley National Laboratory work) results in a large potential drop due to the resistivity of the wafer. When applying sufficiently negative potentials to drive lithiation in the hundreds of $\mu A\ cm^{-2}$ range (as seen in the cyclic voltammagrams in this paper, Figure S7) and a measured resistivity of ~1 kΩ from the contact to the wafer center (where the infrared beam is incident), Ohm's Law tells us to expect a voltage drop of several hundred mV. This is exactly what is observed experimentally in our system as shown in Figure 1.
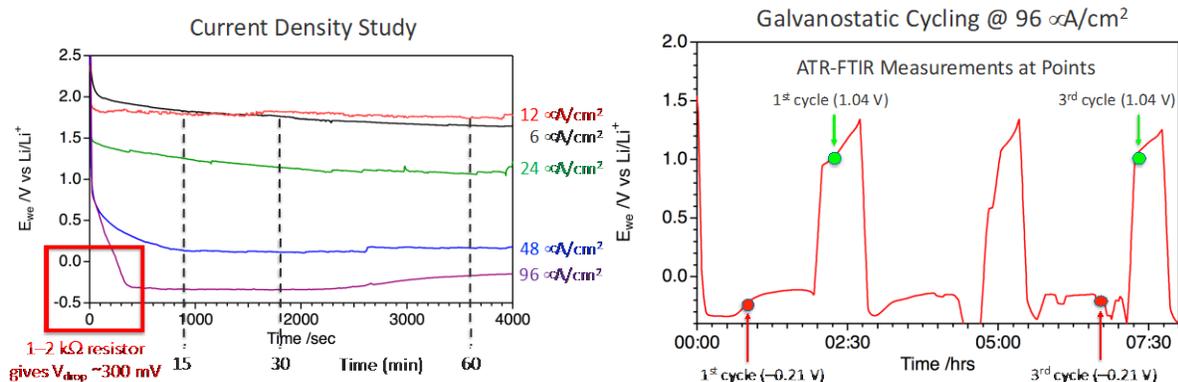
Figure 1. Left: Current density study for 5–10 Ω•cm resistivity Si wafers in the ATR-FTIR spectroelectrochemical cell. A voltage drop of ~300 mV is caused by the resistivity of the low doping density Si wafer. Right: Cycling behavior of the same cell indicating points where ATR-FTIR spectra were collected (see Fig. 2 for ATR-FTIR data).

In Q2, we have eliminated the possibility that there is a contact or other issue based on excellent electrochemical behavior in the *operando* ATR-FTIR cell using the standard high doping density 5 mΩ•cm p^+-Si SEISta wafer as shown in Figure 2. This proves that there is nothing inherently incorrect about the *operando* ATR-FTIR cell for electrochemistry. Spectroscopy, however, is impossible through this high-doping-density wafer as shown in the Figure 2 (middle panel). The blue data show complete absorption of all infrared light in transmittance mode (i.e., single-pass perpendicular to the substrate) for the 5 mΩ•cm p^+-Si SEISta wafer. In contrast, low-doping-density n-Si (red) or low doping density with a highly conductive p-type layers (~10^{19} cm^3 on both sides of wafer) termed p^+n-Si (green) all transmit infrared light. In ATR mode, however, the right panel shows that the beam is absorbed owing to the angle of incidence (30°–80°) and the necessity of making two passes through the wafer. These data mean that, although good electrochemistry is possible, a new methodology of resolving the low conductivity of substrates is needed. In Q3, we will be working on doping a thin, controlled surface region (~1 μm to ~10^{18} cm^3 on only one side of the wafer) to impart high conductivity suitable for electrochemistry with infrared transmittance necessary for ATR-FTIR. An additional approach we are pursuing is to deposit a metal grid line on the back side of the 5 Ω•cm Si wafer to minimize its resistivity.
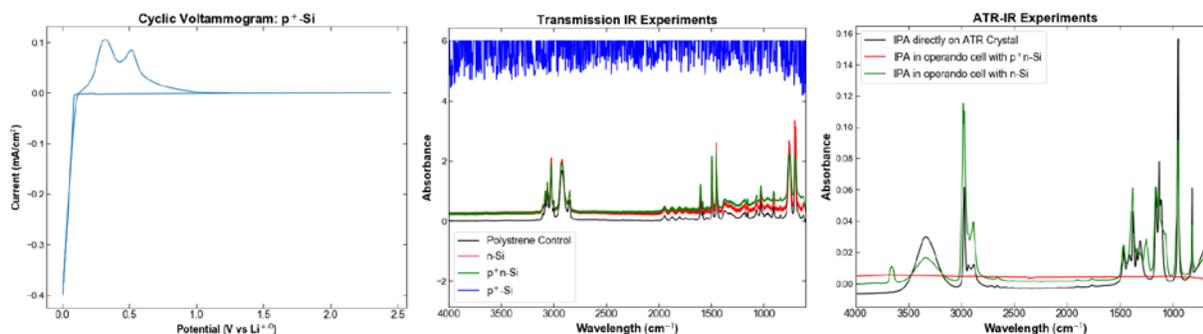
Figure 2. Left: Electrochemical voltammagram conducted in the *operando* ATR-FTIR spectroelectrochemical cell data for native oxide SiO_x|c-Si 5 mΩ•cm p+-Si wafer in Gen2 electrolyte in a half-cell configuration. Middle: Transmittance-mode FTIR data for 5 Ω•cm n-Si (red), 5 Ω•cm p+n-Si with p+ high doping on both sides of the wafer (red), and 5 mΩ•cm p+-Si (blue) wafer. Right: ATR-FTIR data for the same 5 Ω•cm n-Si (this time, color switched to red) and 5 Ω•cm p+n-Si with p+ high doping on both sides of the wafer (this time, color switched to green).

On the complementary reactivity study described over the past two years, we additionally started writing the manuscript in earnest and will be providing a draft to the co-authors including Gabriel Veith (ORNL), Chris

46

Apblett (SNL), and Kristin Persson (UC Berkeley) early in Q3 FY19 (likely at the face-to-face Si Anode Consortium meeting at ORNL 17–18 April).

Silicon Nanoparticle Production via Nonthermal Plasma Synthesis. In FY18, we found that our capacitively coupled plasma (CCP) system could be used to generate 19.9±3.7 nm NPs. Subsequent efforts to optimize growth conditions using this CCP system did not increase Si NP size far beyond an average of 20 nm in FY18. Midway through Q1 FY19, a white paper to expand and accelerate the plasma growth process was accepted by DOE. The PI was notified that funds arrived on 8 November, but funds still have not arrived at Q2 FY19 end. With the assurance of the PI Burrell, we have carried on with the plan outlined in the white paper and have recruited, hired, and begun training a full-time growth technician (Fernando Urias-Cordero) as our first deliverable for this new project.

Additionally, we have worked extensively on a collaborative effort with John Zhang (ANL). NREL has supplied plasma-prepared Si NP samples to enable his surface chemistry work using polyether epoxide ligands, which were hoped to provide good Li-ion transport (via the polyether functionality) as well as chemically binding to the PAA binder (via ring-opening of the epoxide). In Q2, we provided several additional samples as well as co-wrote a manuscript that is the process of being submitted ("Tailoring the Surface of Nano Silicon Particles for Enhanced Chemical and Electrochemical Stabilities in Li-ion Batteries," S. Jiang, B. Hu, R. Sahore, H. Liu, G. M. Carroll, G. F. Pach, L. Zhang, B. Zhao, N. R. Neale, Z. Zhang).

On our efforts to increase the Si NP size and scale, we have had some additional successes. We modified the plasma-reactor conditions in ICP mode to produce 40.6±6.2 nm diameter Si NPs, a huge volumetric increase over our prior Q1 result of 24.5±7.0 nm diameter Si NPs (Figure 3). The drawback is that the conditions used to prepare these larger-diameter samples also resulted in a very low yield. Significant effort in Q3 will be spent increasing the yield of large-diameter Si NPs.
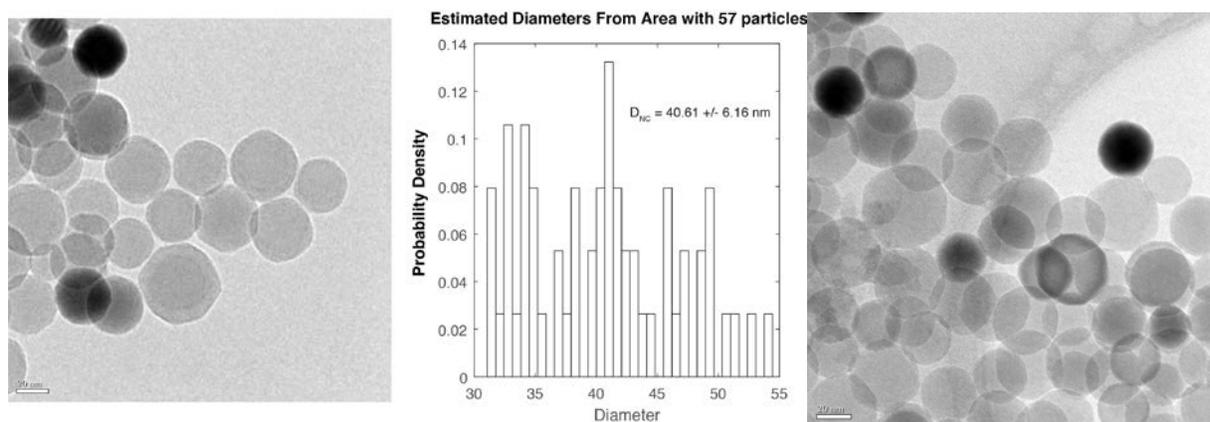
Figure 3. Left and Right: TEM images of SiNPs grown by inductively coupled plasma (ICP). Middle: Size histogram of ICP-synthesized Si NPs showing 40.6±6.2 nm diameters with all particles >30 nm.

Understanding the Role of Silicon Dioxide and Other Si NP Surface Chemistries in Silicon NP Batteries. In an expansion of this portion of the SEISta project, a major effort in FY19 will be spent correlating SEI early-stage growth and dissolution with performance of Si NPs in batteries. Our goal is to study surface-functionalized Si NPs fabricated into batteries *air-free*, and in doing so, to understand how the Si NP surface bonding structure impacts the evolution of the SEI and stability of the electrodes as well as deconvoluting the impacts of oxide versus surface chemistry.

In Q2 FY19, we collected our first data comparing ~150-nm-diameter Paraclete 4KD F17-021-LS with ~7-nm-diameter Si NPs prepared in our plasma process. Notably, these Si NPs are H-terminated. Slurries were prepared using in-house purified polyacrylic acid (PAA) binder and dried Timcal C45 in purified N-methyl-2-pyrrolidone (NMP) solvent. Slurry compositions of the paraclete electrodes were 80%:20%:10% Si:C45:PAA.

Slurries of the plasma-grown Si NCs were varied between 20%–70% Si:70%-20% C45:10% PAA. All slurries were stirred in the Ar-filled glovebox while heating at 70°C for 12–24 h. Electrodes were fabricated by blade casting the prepared slurry onto a Cu current collector inside of a glovebox. The casts were dried at 120°C and then transferred to a vacuum oven and vacuum-dried at 150°C for 3 h. Half cells (Si composite/Celgard/Li metal) were assembled from areal-normalized punches of the composite electrode. The electrolyte was 90% Gen2 and 10% FEC. There were three forming cycles at C/20 between 1.5 and 0.1 V. The measurement cycling protocol is 1 C between 1.5 V and 0.1 V.

We found firstly that the high chemical reactivity (described in many prior reports) of the as-grown, H-terminated Si NPs must be mitigated prior to slurry formation. Pre-treating the Si NPs in NMP solvent (to mimic experiments on ball-milling Si in NMP by Gabriel Veith at ORNL) prior to electrode fabrication generated much higher capacity compared with untreated Si NPs as shown in Figure 4, left panel.

A second key result is that a much higher Si:C45 ratio of 1:3 (cf. 7:1 for Paraclete) is required to fully contact (electrically) the Si NPs. This likely is a function of the small Si NP size as well as the heterogeneity in the slurry that does not allow intimate mixing between the C45 and Si NPs. As such, the capacity over 100 cycles is lower for the 7-nm Si NPs versus Paraclete (Figure 4, middle panel). Importantly, the coulombic efficiency of the electrode made from plasma-prepared Si NPs is equivalent to that of Paraclete over the three C/20 formation cycles and at 1 C rate is lower for the first ~20 cycles but then is superior, approaching 99.5% coulombic efficiency after 100 cycles (Figure 4, right panel). Clearly these are not optimized electrodes, but should provide valuable initial data on studying the effect of oxidation (i.e., preparing similar electrodes not in NMP under air-free conditions but in water as is done conventionally).
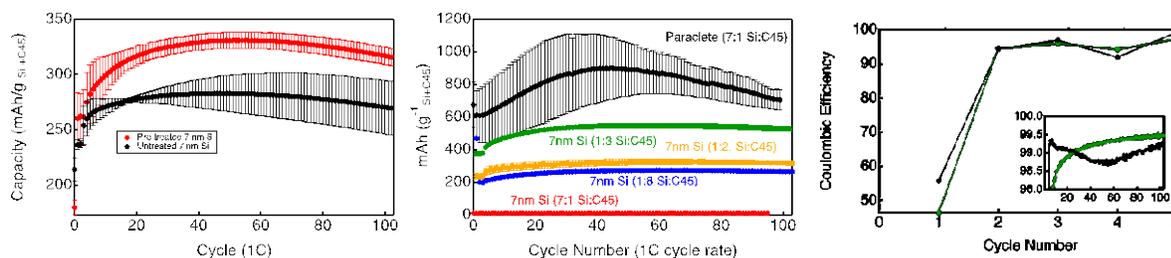
Figure 4. Left: Effect of pre-treating plasma-grown Si NPs in NMP to mitigate chemical reactivity. Middle: Comparison of air-free electrode samples in half-cell configuration between Paraclete Si NPs and plasma-grown Si NPs with varying ratios of C45. Right: Coulombic efficiency data for 7:1 Paraclete:C45 (black) and 1:3 plasma Si:C45 (green).

Further, in Q3, we plan to take these air-free data and conduct a direct comparison to electrode samples prepared under air. This will provide data that address the SEISta milestones comparing pristine surfaces (H-terminated versus native SiO_x-terminated). We also plan to generate a set of polyether-functionalized Si NPs given our previous work on chemical reactivity showing that silyl ether moieties (Si–O–C) are stable chemically toward Gen2 electrolyte. Additional surface-chemistry directions in Q3 include using boron-doped silicon (B:Si) NPs that exhibit solubility in polar solvents such as NMP and water. Finally, we will conduct a size-dependence study to examine the capacity (mAh g^{-1} Si+C45). This should have two functions: 1) determine whether the initial ~20-cycle low coulombic efficiency is due to the high surface area of these small-diameter Si NPs, and 2) increase the Si NPs:C45 ratio to more closely match the Silicon Deep Dive-optimized 7:1 ratio, providing for better comparison. In this way, we might provide a *quantitative* measure of the optimal size for both unoxidized and oxidized Si NPs.

Conclusions

Summary of Q1 FY19 is as follows:

- Re-engineering of the ATR-FTIR spectroelectrochemical cell focused on developing a conductive, infrared-transparent Si wafer substrate. Once operational, the *operando* ATR-FTIR spectrochemical

instrument will be leveraged to understand SEI growth and dissolution on model SEISta planar samples for pristine, native oxide, and surface-functionalized samples in Gen2 electrolyte, both with and without 100 ppm water in direct support of FY19 SEISta milestones.

- Inductively coupled plasma synthesis provides large-diameter Si NPs but at low yield relative to capacitively coupled plasma.
- Hired and now training a full-time growth technician to accelerate development of the plasma growth process.
- Initial dataset on air-free electrodes from plasma-synthesized Si NP have been tested. Planned studies for FY19 include separating the effects of oxidation and surface chemistry on SEI formation and stability in both batteries as well as *operando* ATR-FTIR experiments.

References

[1] Shi, F.; Ross, P. N.; Zhao, H.; Liu, G.; Somorjai, G. A.; Komvopoulos, K. *J. Am. Chem. Soc.* **2015**, *137*, 3181.

[2] Shi, F.; Ross, P. N.; Somorjai, G. A.; Komvopoulos, K. *J. Phys. Chem. C* **2017**, *121*, 14476.

[3] Bapat, A.; Perrey, C. R.; Campbell, S. A.; Carter, C. B.; Kortshagen, U. *J. Appl. Phys.* **2003**, 94, 1969.

SEISta – Fluorescent Probes (NREL) (FY19 Q2)

Contributors: Wade Braunecker, Shriram Santhanagopalan, Kae Fink

Background/Previous Work

In Q1 FY19, we reported on our study of the fluorescent properties of our small-molecule Li sensors under different relevant conditions (under basic vs. pH neutral vs. acidic conditions, and fluorophores with electron-donating vs. -withdrawing groups). The sensors were several orders of magnitude more sensitive under basic conditions as compared to pH neutral, and they had virtually no fluorescence response under acidic conditions. Furthermore, sensors with electron-donating groups ($-CH_3$ or -phenyl) were also orders of magnitude more sensitive to detecting Li than those with electron-withdrawing groups (-CN and -COOR). The results helped us to design appropriate conditions/strategies for applying a fluorescent "stain" to the surface of the SEI.

In Q2, we report on our synthesis of this stain, as well as some critical cyclic voltammetry experiments to determine potential stability windows of the fluorophores under cycling conditions.

Results

1)   Fluorescent Li-detecting gel "stain." Our first attempts to use our small-molecule fluorophore as a surface stain for detecting Li were not successful because suitable solvents could not be found that would prevent the stain from simply dissolving off the surface. By tethering the fluorophore to an acrylic polymer, we could largely solve the problem of dissolution of the stain, but it was no longer sufficiently ionically conductive to drive Li ions in and out of the material without degrading. Thus, we synthesized a PMA/PEG-based gel electrolyte that includes a tethered fluorophore (**Fig. 1**). The material is ionically conductive if loaded with Na ions, and in principle, fluorescence will turn on when Li ions are driven into the material, e.g., from or through a Si SEI layer.

Following the synthesis of a vinyl-containing analog of the fluorophore (2-hydroxyphenyl) napthoxazole (or **HPNO**), we tethered 2 mol% of this molecule into polymethylacrylate, PMA, using conventional radical polymerization. After purification of the material and basic characterization using 1H nuclear magnetic resonance (NMR), we also performed detailed size-exclusion chromatography analysis of the new copolymer (Fig. 2) to conclusively determine that ~100% of the HPNO fluorophore present in the final material was indeed covalently tethered to the polymer. This polymer can now simply be blended with PEO and $NaPF_6$ to create the gel stain proposed in Fig. 1. Electrostatic crosslinking should keep the polymer from dissolving into liquid electrolyte under cycling conditions, but it may be necessary to add a small amount of a standard ultraviolet-activated crosslinking agent to ensure no dissolution of this stain into liquid electrolyte.
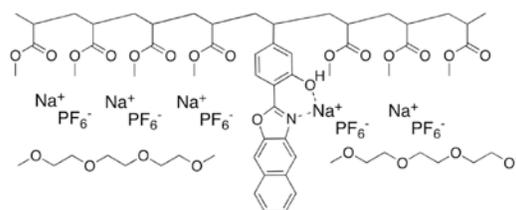
Figure 1. PMA/PEG Na-based gel electrolyte. Material has good processability and ionic conductivity. Fluorescence will "turn on" when Li+ is driven into the material and replaces Na+.
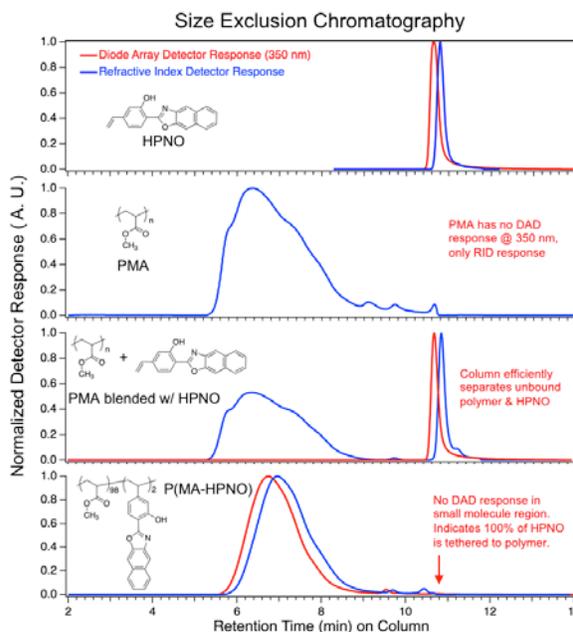
Figure 2. SEC analysis determines HPNO is definitively tethered to polymer backbone.

This system will allow us in principle to flow/deposit a homogeneous layer of conductive gel electrolyte onto the SEI layer at high temperatures; afterwards, we will cool the electrolyte to "fix" it in place and attempt to cycle the system one time and drive Li from the anode through the SEI and into our electrolyte gel, with the goal of ultimately imaging the flow of Li through our fluorophore-containing electrolyte as it displaces Na.

2) Cyclic Voltammetry (CV). With a target material now designed and in hand, we assessed the cycling stability of the material, including its "window" of operation, under several relevant conditions. The stability of HPNO was assessed across the wide voltage range 0–4.5 V *vs*. Li metal in the following solutions:

> (1) LiPF$_6$ (1.2 M) in EC:EMC (3:7 by weight) ("Gen2," commercial)
> (2) NaPF$_6$ (1.2 M) in EC:EMC (3:7 by weight) (synthesized in-house)
> (3) Tetraethylammonium tetrafluoroborate (TEABF$_4$) (0.9 M) in EC:EMC (1:1 by weight)
>   (synthesized in-house). *Note: TEABF$_4$ was insoluble in 3:7 formulation of EC:EMC, so ratios*
were
>   *adjusted until solubility was achieved.*

Furthermore, CV was conducted at several scan rates (600 µV/s to 50 mV/s), and the performance of dilute solutions of HPNO in each electrolyte was compared to a "blank" of the corresponding electrolyte solution.
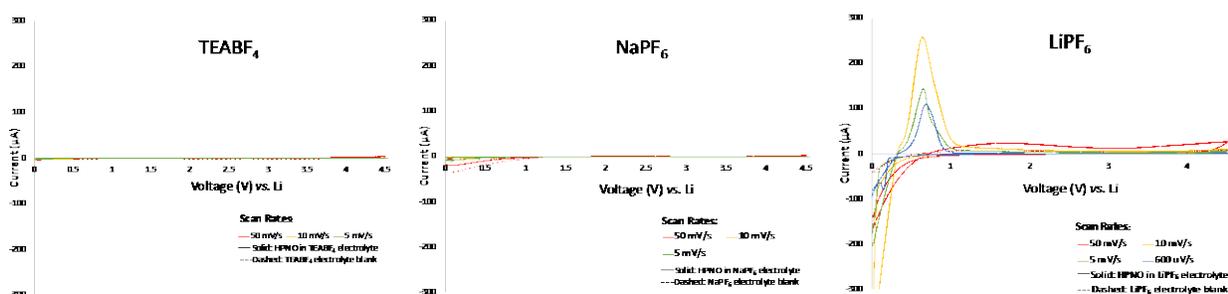
Figure 3. Variable scanning rate CV for a solution of HPNO in three different electrolytes.

The results indicate that the HPNO molecule is quite stable in the non-coordinating TEABF$_4$ electrolyte, as well as the NaPF$_6$ electrolyte, across the full voltage range 0–4.5 V *vs*. Li metal, over a range of different scanning speeds. Interestingly, it is also stable at faster scanning rates (> 50 mV/s) in the LiPF$_6$ "Gen2" electrolyte; but at slower scanning rates (10 mV/s and slower), there is an irreversible reaction peak observed at ~0.65 V (Figure 3C). It seems this may correspond to Li/HPNO binding because it does not occur in the other systems, and it further implies a relatively slow reaction. We are currently attempting to analyze the effects of the cycling on chemical composition using gas chromatography/mass spectrometry to better understand the decomposition that is occurring under specified conditions.

Conclusions

Significant progress was made toward developing Li-ion sensors for application as a fluorescent "stain" on an SEI layer. The HPNO molecule was definitively tethered to a polymeric backbone. We developed that polymer into an ionically conductive system. Furthermore, having completed a series of CV experiments, we have a much better understanding of conditions required to sense/image Li. We are actively discussing the outcome of these results with several NREL researchers and their full implications on our next steps in the SEISta program, as well as what range of other possible systems these materials may find application.

Silicon Model Compound – Electrolyte Reaction Studies

J. Vaughey, N. Sa, S. Cora, S. Ahmad, B. Han, B. Key

Background

In the FY18 SEIsta round-robin study on the use of silicon thin films as model compounds for studying silicon electrodes under various controlled conditions, one of the uses—besides lab-to-lab consistency and storage effects—was their use as model electrodes for SEI studies. We used electrochemical quartz-crystal microbalance (EQCM) spectroscopy to study these silicon films; we evaluated the role of silica surfaces and coating thickness on electrochemical stability; and we continued by looking at the properties of SEI films formed in the cell on cycling. This work highlighted that the SEI formed in Gen2 electrolyte was relatively porous (low density) and changed weight during the charge and discharge cycles. On addition of FEC (a common electrolyte film-former added to silicon systems) and cycling, the SEI became more compact and dense. This has been assigned to various attributes of the FEC molecule opening and the role of fluoride incorporation in the film. In this quarter, we have continued these studies based on observation that since FEC is added as a co-solvent with no salt molarity correction, the conductivity of the electrolyte is not being held constant during the measurements.

Results

Among lithium-ion battery silicon researchers, the electrolyte additive of fluoroethylene carbonate (FEC) is typically used at 10 wt% in Gen2 (3:7, EC/EMC, 1.2M $LiPF_6$) by researchers in the program. In the electrolyte, the FEC is thought to undergo a ring-opening reaction with loss of fluoride (to LiF) and produces a stable conductive film. This film has been found to support fast ionic conductivity of lithium, but it has a limited lifetime in the system (especially when compared to a vinylene carbonate-derived film); and once the free monomer is consumed, its performance degrades.[1,2] We have previously used EQCM spectroscopy to analyze this film process and noted that the addition of FEC significantly densifies the SEI layer. This quarter, we report on two variables to understand this process—nominally, the initial film-formation step and the conductivity of the electrolyte.

In a continuation of our nuclear magnetic resonance (NMR) studies, we have examined the degradation mechanism of FEC in the presence of Li_7Si_3, our model compound for a 300-mV Li_xSi electrode. In this report, we mixed the model compound with FEC and soaked it for three days. ^{19}F and ^{7}Li NMR studies on the recovered samples indicated that little if any LiF was produced (see ^{19}F NMR), whereas the slight shift in the ^{7}LiNMR indicated that a reaction had occurred. Combined, we conclude that although FEC is thought to reduce in solution > 1 V (vs Li), we see little evidence at our ~300 mV that the ring opening involves fluoride abstraction, even when the average oxidation state of the silicon has changed.
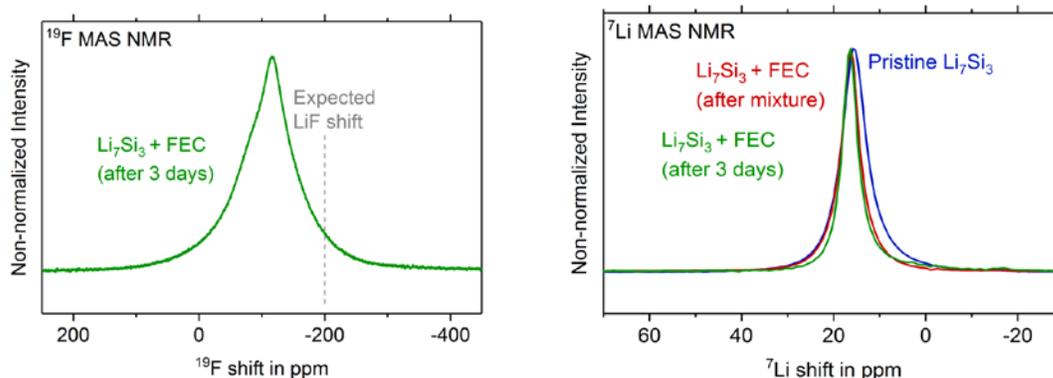
Figure 1. ^{19}F and ^{7}Li MAS NMR spectra of the product mixture from the mixture of Li$_7$Si$_3$ and FEC after three days of exposure. Dashed line in the ^{19}F spectra indicates the expected location of LiF.

Last year, we noted that although FEC addition is relatively ubiquitous for lithium-silicon electrochemistry, all of the roles the FEC plays in the electrolyte were undefined. The amount of FEC added commonly seen in the literature (and consistent with our previous (Q1 FY18) study) is near the point of maximum beneficial effect, near the range 5–20 wt%. However, because the FEC itself is a co-solvent, adding FEC to the Gen2 electrolyte will change the concentration of LiPF$_6$. Thus, the electrochemical response is a combination of the added FEC (as the Persson group has noted in their studies that it changes the stable solution species) and the decrease in LiPF$_6$ salt concentration upon dilution with FEC. This quarter, we studied the effect on solution conductivity of Gen2 electrolyte with various amounts of added FEC. Table 1 and Figure 1 show the actual LiPF$_6$ concentration as an effect of adding FEC from 0%, 5%, 10%, 15%, and 20%. Quick calculations show that upon addition of FEC as a co-solvent, the LiPF$_6$ concentration drops from 1.2 M to 1.0 M—a ~17% decrease in molarity (see Table 1). To level the salt molarity in the system so as to study FEC addition without changing conductivity, we added an appropriate amount of LiPF$_6$ to adjust the concentrations to 1.2 M. For sample volumes used (3 mL), the electrolyte samples needed to have an additional 0.024–0.085 g of salt added, depending on the amount of FEC added (see Table 1). Work in underway to determine the conductivity values as differences in coordination environment and stable species are known; the 1.2M value was set as the point of maximum conductivity in the Gen2 electrolyte, so some decline is expected.

Table 1. Effect of FEC addition to the concentration of LiPF$_6$

Sample number	FEC w.t.%	Mass of FEC (g)	Mass of Gen2 (g)	Volume of FEC (ml)	Total volume (ml)	Initial Concentration of LiPF$_6$ (M)	Real concentration of LiPF6 (M)
1	0%	0	3.900	0	3 ml (3.9 g)	1.2 M	1.200
2	5%	0.195	3.705	0.138	3 ml (3.9 g)	1.2 M	1.147
3	10%	0.390	3.510	0.277	3 ml (3.9 g)	1.2 M	1.099
4	15%	0.585	3.315	0.415	3 ml (3.9 g)	1.2 M	1.054
5	20%	0.780	3.120	0.553	3 ml (3.9 g)	1.2 M	1.013
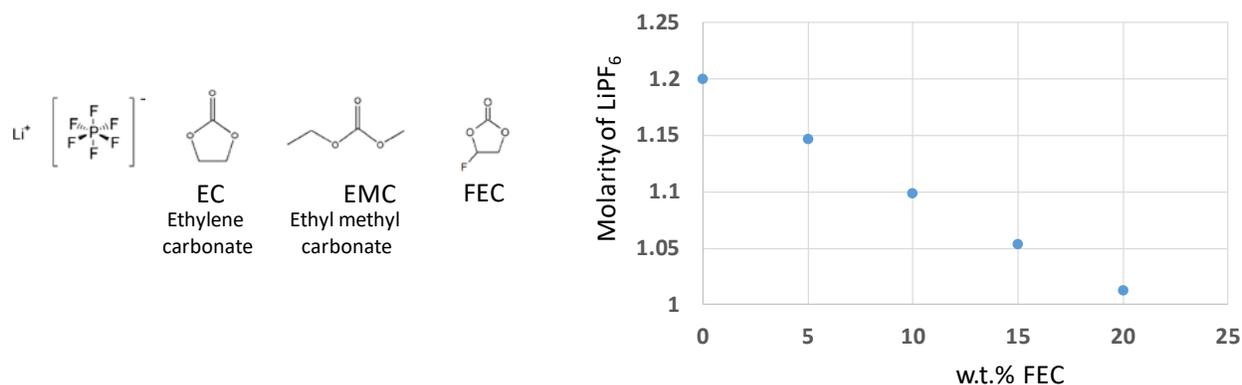
Figure 2. LiPF$_6$ molarity with FEC addition in wt percentage from 0%, 5%, 10%, 15%, and 20%.

Conclusions

We continue to examine the role of reduced silicon materials in the electrochemical systems. We have looked at the role of the common electrolyte additive FEC and noted that the film-forming mechanism commonly reported (but not universally accepted) based on LiF formation was not supported by multi-nuclear NMR studies. In ^{19}F and ^{7}Li NMR analysis—after cyling and in a voltage window where ring opening was occurring—no evidence of LiF was seen, although reactions did occur. These data are consistent with the formation of a fluoro-containing polymer possibly similar to a substituted polycarbonate. In the second study, we initiated a study on the role of diluting the electrolyte with FEC while not compensating for the drop in salt molarity. Compared to literature values, the conductivity should be affected by the nearly 20% drop in salt concentration.

References

[1] T. Jaumann, J. Balach, U. Langklotz, V. Sauchuk, M. Fritsch, A. Michaelis, V. Teltevskij, D. Mikhailova, S. Oswald, M. Klose, G. Stephani, R. Hauser, J. Eckert, L. Giebeler, "Lifetime vs. rate capability: Understanding the role of FEC and VC in high-energy Li-ion batteries with nano-silicon anodes," *Energy Storage Materials*, **6**, 26–35 (2017).

[2] Y. Jin, N.-J. H. Kneusels, L. E. Marbella, E. Castillo-Martínez, P. C. M. M. Magusin, R. S. Weatherup, E. Jónsson, T. Liu, S. Paul, C. P. Grey, "Understanding Fluoroethylene Carbonate and Vinylene Carbonate Based Electrolytes for Si Anodes in Lithium Ion Batteries with NMR Spectroscopy," *J. Am. Chem. Soc*. **140**, 9854−9867 (2018).

Quantitative Liquid-State NMR Results on Soluble SEI Products

Baris Key (ANL), Gabriel Veith (ORNL), Bob Jin Kwon (ANL), Jack Vaughey (ANL)

Background

Understanding the dissolution phenomena of the silicon-electrolyte interphase (SEI) in common electrolytes used is essential in stabilization of the SEI and preventing active Li inventory losses. One of the goals of the SEISta program is to establish and demonstrate procedures to quantitatively measure the solubility of SEI on silicon surfaces. To this end, spectroscopic characterization protocols have been developed to study the early-stage SEI formation on the SEISta model research samples.

Results

Standard SEISta test half-cells were assembled with Gen2 electrolyte using silicon wafers with amorphous silicon to produce and evolve the SEI for 1 cycle, and the electrolyte is sampled in inert conditions for solutions nuclear magnetic resonance (NMR) characterization. Figure 1 shows ^{19}F solutions NMR spectra of cycled SEISta standard Gen 2 electrolyte (red) and baseline Gen2 (black). Both spectra show the standard PF_6^- doublet centered at -74 ppm. The cycled sample in addition shows a doublet centered at -85 ppm, which is ascribed to PO_xF_y (specifically assigned to $PO_2F_2^-$) species due to PF_6^- decomposition with 0.65 mol % concentration vs. PF_6^- in the electrolyte, i.e., a concentration of 750 ppm.[1] Free F^- dissolved in the electrolyte was also detected via a peak at -190 ppm after one cycle, indicating HF presence with a 1.3 mol % concentration vs. PF_6^- in the electrolyte, i.e., a concentration of 300 ppm. These results mainly show the electrolyte self- and impurity (H_2O)-driven electrochemical decomposition products with preliminary quantification.
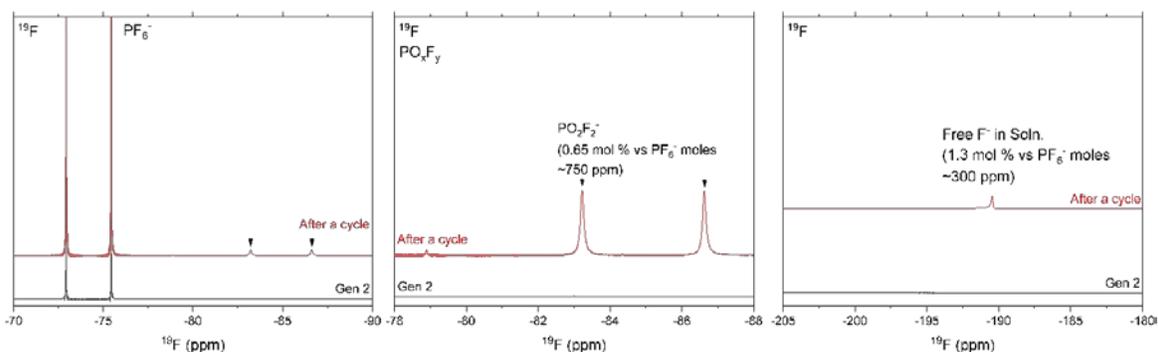
Figure 1. ^{19}F NMR spectrum of cycled SEISta standard Gen2 electrolyte (red) and baseline Gen2 (black). Argonne National Laboratory (ANL), unpublished results.

To probe SEI solubilization quantitatively, ^{7}Li, ^{1}H, ^{29}Si, and ^{13}C NMR measurements were performed on the sample and the baseline. No peaks were detected in ^{29}Si NMR (data not shown), indicating no significant solubilization of silicon-bearing species. ^{7}Li NMR in Figure 2 shows no major changes, mainly due to the overlap of diamagnetic Li peaks. ^{13}C NMR results show, in addition to the solvent molecules in the electrolyte (EMC and EC), new lithium-bearing carbonates species in the 155 to 170 ppm region.[2-4] The small peak at ~155.5 ppm is ascribed to LiEDC, with a 1.4 mol % concentration vs. EC in the electrolyte, i.e., a concentration of 10,000 ppm. The small peak at ~156.5 ppm is ascribed to LiEC, with a 0.4 mol % concentration vs. EC in the electrolyte, i.e., a concentration of 1,700 ppm. These two initial assignments cannot rule out contribution from LiBDC. Corroborating changes were observed in ^{1}H NMR (data not shown). Another small peak at a higher frequency is tentatively ascribed to Li_2CO_3 with a 0.3 mol % concentration vs. EC in the electrolyte, i.e., a concentration of 990 ppm; but it must be noted that the concentrations are fairly high because low solubilities are expected for lithiated carbonates in the electrolyte.[5]
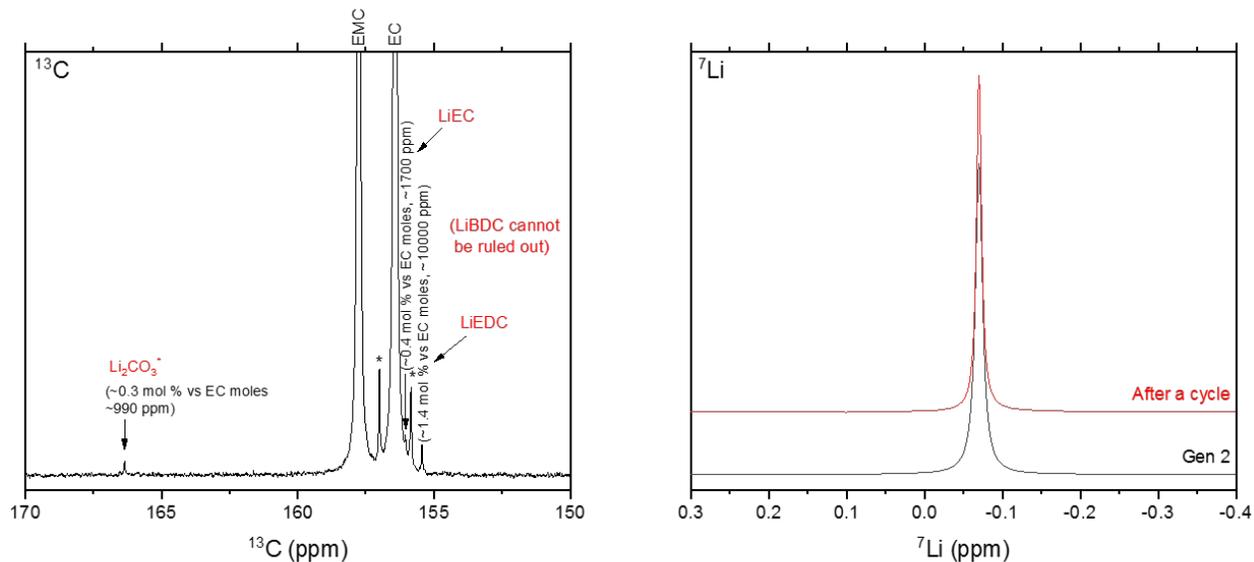
Figure 2. ¹³C and ⁷Li NMR spectra of cycled SEISta standard Gen2 electrolyte and baseline Gen2. ANL, unpublished results.

Conclusions

A protocol for quantitatively measuring soluble SEI products in standard SEISta research samples is established using NMR spectroscopy. The findings suggest significant electrolyte decomposition and lithium-bearing SEI species solubilization in the electrolyte. For precise quantification, internal standards are planned to be used in the future. Extended cycled standard cells will be analyzed to monitor the buildup of the identified and/or new species.

References

[1] K. Tasaki, K. Kanda, S. Nakamura, M. Ue, *Journal of the Electrochemical Society*, 2003, 150 (12), A1628–A1636
[2] A. L. Michan, M. Leskes, C. P. Grey, *Chemistry of Materials*, 2016, 28, 1, 385–398.
[3] J. Li, W. Yao, Y. S. Meng, Y. Yang, *Journal of Physical Chemistry C*, 2008, 112, 32, 12550–12556.
[4] Y. Jin, N. H. Kneusels, L. E. Marbella, E. Castillo-Martinez, P. C. M. M. Magusin, R. S. Weatherup, E. Jonsson, T. Liu, S. Paul, C. P. Grey, *Journal of the American Chemical Society*, 2018, 140, 31, 9854–9867.
[5] K. Tasaki, A. Goldberg, J. Lian, M. Walker, A. Timmons, S. J. Harris, *Journal of the Electrochemical Society*, 2009, 156 (12), A1019–A1027